Computational Investigation of the Catalytic Hydrodeoxygenation of Propanoic Acid over a Cu(111) Surface

Biplab Rajbanshi,† Wenqiang Yang, Adam Yonge, Subrata Kumar Kundu, Charles Fricke and Andreas Heyden*

Department of Chemical Engineering, University of South Carolina, 301 South Main Street, Columbia, South Carolina 29208, USA.

E-mail: heyden@cec.sc.edu

*To whom correspondence should be addressed

†Current address: Department of Chemistry, Visva-Bharati University, Santiniketan-731235, India.

ABSTRACT:

Cu-based alloy catalysts have recently been investigated experimentally for the hydrodeoxygenation (HDO) of biomass derived organic acids. Here, the HDO of propanoic acid (PAc) has been studied over Cu(111) by mean-field microkinetic modeling based on parameters obtained from first-principles calculations. Models were developed for the gas- and liquid-phase HDO in condensed water and 1,4-dioxane. In agreement with experimental observations, the gas-phase PAc conversion rate is low at 573 K and increases in liquid water by one order of magnitude. In all reaction environments, the decarboxylation mechanism is dominant at low hydrogen partial pressures less than 0.1 bar, and the C-COO bond dissociation is the rate-controlling elementary step. This observation contrasts with the rate-controlling step identified over most Group VIII metal surfaces, which is the C-OH bond dissociation in the decarbonylation mechanism. At high hydrogen (H_2) partial pressures greater than 10 bar, the HDO of PAc produces propionaldehyde that can re-adsorb and further react through decarbonylation to produce C_2 alkane products, which is conceptually different to the low H_2 partial pressure scenario. At high H_2 partial pressure, the initial hydrogenation at the carbonyl carbon of PAc becomes the rate controlling elementary step.

1. INTRODUCTION

The use of fossil resources for the generation of transportation fuels and chemicals is accompanied by increasingly adverse environmental consequences.[1] Thus, conversion of renewable carbon sources such as biomass continue to be investigated for the generation of fuels and chemicals.[2-4] Bio-oils and lipid-rich biomass feedstocks contain large amounts of oxygenates such as organic esters and carboxylic acids that are highly corrosive and challenging to deoxygenate to conventional hydrocarbon fuels.[5-8] Converting these biomass feedstocks into high-quality transportation fuels requires some of the oxygen atoms to be removed from the feedstock molecules. Catalytic hydrodeoxygenation (HDO) of biomass-derived carboxylic acids and esters is a possible process for the generation of drop-in fuels.[2, 9-12] Recent research has explored the HDO of propanoic acid (PAc), a surrogate molecule for "larger" carboxylic acids, over various supported noble metal catalysts. Of those noble metals investigated, Ru, Rh, Pd, Pt, and Ir exhibited a high activity.[13-23] For example, Lugo-José et al. studied the gas-phase HDO of PAc over SiO_2 supported group VIII noble metal catalysts at 200-400 °C and atmospheric pressure.[19]

They observed a reaction activity order of Pd>Ru>Pt>Rh>Ni, and that hydrocarbons were the main reaction product formed through decarbonylation (DCN) and decarboxylation (DCX) pathways.[19] In another study of carbon supported metal catalysts for the HDO of PAc at 200 °C and 1 atm total pressure, Lugo-José observed an activity order of Rh=Pt>Ir>Ru=Ni=Pd for the production of alkanes, specifically ethane.[24] Similarly, Olcay et al. studied the aqueous-phase hydrogenation of acetic acid (AAc) over transition metal catalysts at 110-290 °C and 5.17 MPa pressure; and they found an activity order based on turnover frequencies (TOFs) of: Ru > Rh ≈ Pt > Pd ≈ Ir > Ni > Cu with ethanol as the main reaction product.[20] Recently, we have computationally explored the HDO of PAc to C_2 alkanes on Pd, Ru, and Ni metal surfaces by a combination of density functional theory calculations and microkinetic modeling. In these studies, we found that the DCN pathway is preferred over the DCX pathway.[25-31] In another study, we observed alcohol and aldehyde formation in addition to decarbonylation products during the vapor phase HDO of PAc over a Pt surface.[32] In condensed phase reaction environments, the reaction products shift away from alkanes towards alcohols and aldehydes. In contrast, in a recent study we found that the HDO of PAc over Rh(111) mainly produces propanol and propionaldehyde in both vapor and liquid phase environments, and both DCN and DCX do not occur at an appreciable rate in any reaction environments.[33] Although noble metals (Pd, Pt, Rh, and Ru) generally show an appreciable activity towards the HDO of PAc, their high cost restricts their usage.[34-35] Thus, there is a desire to use more earth abundant elements for the design of more active HDO catalysts. Recently, Cu metal catalysts have been studied for CO hydrogenation,[12, 36-40] CO_2 hydrogenation,[41-42] formic acid dehydrogenation,[43-44] AAc hydrogenation,[20, 45-47] and the HDO of PAc.[24] For example, Olcay et al. reported for the aqueous phase hydrogenation of AAc that Cu offers a 59% selectivity towards acetaldehyde (EtCHO) and 41% selectivity to ethyl acetate at a relatively low TOF of 1×10^{-3} h^{-1} at 150 °C. At a higher temperature of 260 °C, the TOF increased to 3×10^{-1} h^{-1} with 75% selectivity towards ethanol.[20] For the vapor phase HDO of PAc over a Cu/C catalyst at 300 °C, Lugo-José observed a 70% selectivity towards C2 hydrocarbons and a 29% selectivity towards EtCHO.[24] No alcohol formation has been reported at any temperature for the vapor phase HDO of PAc over the Cu/C catalyst and given the overall low rate, Lugo-José hypothesized that at least some of the observed activity might originate from the carbon support.[24] Although the catalytic performance of Cu for all of these reactions was lower than that observed for the noble metals, Cu also displays an extremely low selectivity towards CO which is a typical

catalyst poison.[43-44] Furthermore, given that even small amounts of CO cover/block (together with adsorbed hydrogen) large portions of the active surface of noble metal catalysts during the HDO of PAc,[25-28, 30, 32] the low CO production rate and weak binding of CO on Cu surfaces might suggest that Cu-based alloy catalysts could become a platform for novel HDO catalysts of organic acids. In this context, a Cu_3Pt alloy has been predicted to be as active as the precious metals Ir, Pd, Pt, Ru, and Rh for the formic acid decomposition.[44] Zhang et al. have predicted that Ru and Rh dopants might improve the catalytic activity of Cu for the hydrogenation of AAc.[35] And, Crocker et al. have shown that Cu-Ni catalysts are active for the HDO of lipids.[48-50] In order to understand the potential of Cu alloy catalysts for the HDO of organic acids, it is instructive to first better understand the catalytic pathways on Cu itself.

Thus, in this study, we investigated the reaction mechanism of the HDO of PAc over Cu(111). Given that the HDO of organic acids is experimentally often studied in solvents such as liquid water and 1,4-dioxane, we developed microkinetic reaction models for both the vapor phase and the condensed phases of liquid water and 1,4-dioxane. In this way, we attempt to better understand possible solvation effects on rate and selectivity controlling steps. We note that Hoelderich et al. found that liquid water can change the C17 hydrocarbon selectivity by up to 20% in the deoxygenation of oleic acid (C18) over a Pd/C catalyst.[51] Also, we noted previously that decarboxylation pathways are generally facilitated in the presence of liquid water,[25, 27] and that propanol and propionaldehyde production might also be facilitated in condensed media with liquid water displaying the strongest effects.[32]

2. METHODS

2.1. Details of Computation

All gas phase density functional theory (DFT) calculations used the projector augmented wave (PAW) method[52-53] and were performed using the Vienna *ab initio* simulation package (VASP 5.4).[54-56] The Perdew and Wang 1991 functional (PW91) with the generalized gradient approximation (GGA) was used to describe the exchange and correlation terms of DFT.[57-58] The energy cutoff for the plane wave basis sets was 400 eV. All structures were relaxed until the residual force on each atom became less than 0.01 eV/Å, and the self-consistent field (SCF) energy

convergence cutoff was set to 10^{-7} eV. The optimized lattice constant of a Cu unit cell is 3.63 Å, which is in good agreement with the reported experimental value of 3.615 Å.[59] A $3\times2\sqrt{3}$ Cu (111) surface was modeled from the optimized unit cell with four Cu atom layers (48 total metal atoms), i.e., each layer of the Cu(111) metal slab has 12 Cu atoms with surface area of 68.45 $Å^2$ (7.70 Å×8.89 Å) which we found sufficiently large to compute adsorption energies in the low surface coverage limit. A vacuum distance of 15 Å was added normal to the plane to avoid any interaction between the replicas. To sample the Brillouin zone, a 4×4×1 Monkhorst-Pack (MP) k-mesh was used.[60] All of our metal surface calculations were spin polarized.[34-35] For all surface calculations, the top two layers were allowed to relax in all directions while the bottom two layers were fixed in the optimized bulk position. To determine the transition state (TS) of each elementary reaction step a combination of the climbing-image nudged elastic band (NEB),[61-62] and the dimer methods were used.[63-64] The characterization of all the TS as well as minima was done by numerical vibrational frequency calculations with a step length of 0.005 Å. To improve the accuracy of the harmonic approximation we shifted all (real) frequencies below 100 cm^{-1} to 100 cm^{-1}, so that for surface reactions low-frequency modes do not affect reaction energies and rate constants.[28, 32]

To investigate the solvent effect of a liquid on various elementary reactions at least approximately, the implicit solvation model for solid surface (iSMS) method was used. Detailed information about iSMS has recently been published elsewhere.[65] The principal idea of this model is to account for the long-range metal interactions through periodic slab calculations in the absence of solvent and to include the effect of the solvent as a localized perturbation using a cluster model embedded in an implicit continuum solvent. The free energy of an adsorbed surface intermediate on a periodic metal slab in liquid, $G^{liquid}_{surface+intermediate}$, can be described as,

$$G^{liquid}_{surface+intermediate} = G^{vacuum}_{surface+intermediate} + (G^{liquid}_{cluster+intermediate} - E^{vacuum}_{cluster+intermediate}) \quad (1)$$

where $G^{vacuum}_{surface+intermediate}$ is the DFT free energy (harmonic approximation for vibrational contributions) of the surface slab model in the absence of a solvent, $G^{liquid}_{cluster+intermediate}$ is the free energy of a metal cluster in the liquid built by removing selected metal atoms from the periodic slab model and removing the periodic boundary conditions (vibrational contributions are not

considered), while $E^{vacuum}_{cluster+intermediate}$ is the DFT energy of the same cluster model without the solvent. The COSMO-RS implicit solvation model was used to compute $G^{liquid}_{cluster+intermediate}$ with the COSMOtherm program.[66-68] The thermodynamic properties of the solvents are obtained from the COSMOtherm database at the BP/TZVPD-FINE level of theory. The COSMO-RS input files for all the remaining structures have been generated from the COSMO calculations at the same level of theory. Given the uncertainty in the solvent parameters for the Cu metal atoms, the solvent calculations were repeated with a cavity radius that is ±10% of the default Cu cavity to account for the sensitivity of our liquid phase results to the most important Cu solvent parameter.

2.2. Microkinetic modeling

The adsorption free energies, G_{ads}, of all species on the metal surface were calculated with a universal reference according to the following equations:

$$G_{ads} = G_{slab+intermediate} - G_{slab} - (N_C \times E_C) - (N_H \times E_H) - (N_O \times E_O) \quad (2)$$

$$E_C = E_{CH4} - (2 \times E_{H2}) \quad (3)$$

$$E_H = 0.5 \times E_{H2} \quad (4)$$

$$E_O = E_{H2O} - E_{H2} \quad (5)$$

where $G_{slab+intermediate}$ is the free energy of the intermediate on the surface slab, G_{slab} is the free energy of the clean surface slab, and E_{CH4}, E_{H2O}, E_{H2} are the energy of the CH_4, H_2O, and H_2 molecules, respectively. N_C, N_H and N_O are the number of C, H and O atoms in the intermediate. Based on the G_{ads} calculated by equation (2), the reaction and activation free energies are defined as,

$$\Delta G_i^{rxn} = \sum_j \nu_{ij} \times G^i_{ads,j} \quad (6)$$

$$\Delta G_i^{\ddagger} = G^{\ddagger}_{ads,i} - \sum G^R_{ads,i} \quad (7)$$

where ΔG_i^{rxn} and $\Delta G_i^{\ddagger}$ are the reaction free energy and activation free energy of reaction step i, ν_{ij} and $G^i_{ads,j}$ are the stoichiometry coefficient and adsorption free energy of intermediates j in reaction step i, and finally, $G^{\ddagger}_{ads,i}$ and $G^R_{ads,i}$ are the adsorption free energy of the transition state and the sum of the adsorption free energies of the reactant of reaction step i, respectively. The reference state does not affect the free energy calculations.

Next, harmonic transition state theory has been used to calculate rate constants for the elementary surface reactions, i.e., the forward rate constants (k_{for}) of surface reactions were calculated as,

$$k_{for} = \frac{k_B T}{h} e^{-\frac{\Delta G^{\ddagger}}{k_B T}} \quad (8)$$

where $\Delta G^{\ddagger}$ is the zero-point energy (ZPE) corrected activation barrier for the forward reaction obtained from DFT calculations, k_B is the Boltzmann constant, h is Planck constant, and T is the reaction temperature in Kelvin. For adsorption processes, the forward rate constants were calculated using collision theory with a sticking coefficient of 1, i.e.,

$$k_{for} = \frac{1}{N_0 \sqrt{2\pi m_A k_B T}} \quad (9)$$

where N_0 is the number of sites per surface area (1.752×10^{19} m^{-2}) and m_A denotes the molecular weight of adsorbent A. The reverse reaction rate constant (k_{rev}) is determined from the thermodynamic equilibrium constant K,

$$K = \frac{k_{for}}{k_{rev}} \quad (10)$$

The free energy of reaction ($\Delta G^{rxn}_{solvent}$) and activation free energy ($\Delta G^{\ddagger}_{solvent}$) in the presence of solvents were calculated using the following equations:

$$\Delta G^{rxn}_{solvent,i} = G^{rxn}_{gas,i} + G^{solv}_{FS} - G^{solv}_{IS} \quad (11)$$

$$\Delta G^{\ddagger}_{solvent,i} = G^{\ddagger}_{gas,i} + G^{solv}_{TS} - G^{solv}_{IS} \quad (12)$$

where G^{solv}_{IS}, G^{solv}_{FS}, and G^{solv}_{TS} are the solvation free energies of the reactants, transition state, and products of reaction step i, respectively, which were obtained from the COSMO-RS calculations. We note that Zhang et al. recently showed that even in condensed phase environments, collision theory is a meaningful approximation for adsorption processes.[69]

After obtaining the forward and reverse rate constants for each elementary reaction, a mean-field microkinetic model was built for the normalized number of surface species i per surface metal atom.[70] Thus, the surface coverage of each species *i* is equal to the number of sites occupied by the species per surface metal atom times the number of surface metal sites occupied by each species *i*.[32]

In order to understand the temperature dependence of the derived TOFs, the apparent activation energy (E_{app}) was calculated as,

$$E_{app} = k_B T^2 \left(\frac{d\ln(TOF)}{dT}\right)_{P,y_i} \quad (13)$$

keeping the total pressure (P) and the mole fractions of each species *i* in the reaction mixtures (y_i) constant.

The reaction order (α_i) with respect to species *i* at a specific temperature (T) was determined by the expression,

$$\alpha_i = \left(\frac{d\ln(TOF)}{dln(P_i)}\right)_{T,P_{j\neq i}} \quad (14)$$

where the partial pressure (or fugacity) of the species (P_i) was varied while keeping the partial pressures (fugacities) of all other species ($P_{j\neq i}$) constant.

The degree of kinetic rate control ($X_{RC,i}$), degree of thermodynamic rate control ($X_{TRC,n}$), and the selectivity control ($X_{SC,i}$) for each step *i* were calculated using Campbell's theory[71-73] as,

$$X_{RC,i} = \left(\frac{\partial lnr}{\partial \frac{-G_i^0}{RT}}\right)_{G_{j\neq i}^0}, \quad X_{TRC,n} = \left(\frac{\partial\, ln\, TOF}{\partial \frac{-G_n^0}{RT}}\right)_{G_{j\neq n}^0} \quad (15)$$

$$X_{SC,i} = \left(\frac{\partial \ln(\frac{r_P}{r_R})}{\partial \frac{-G_i^0}{RT}}\right)_{G_{j\neq i}^0} = \left(\frac{\partial lnr_P}{\partial \frac{-G_i^0}{RT}}\right)_{G_{j\neq i}^0} - \left(\frac{\partial lnr_R}{\partial \frac{-G_i^0}{RT}}\right)_{G_{j\neq i}^0} = X_{RC,i,P} - X_{RC,i,R} \quad (16)$$

where the standard-state free energy of all other species G_j^0 (intermediates, transition states, reactants, and products) are held constant. The value of $X_{RC,i}$ defines the relative increase in net rate due to the (differential) stabilization of the standard-state free energy for a particular transition state of reaction step *i*, holding all the other species' energies constant, and $X_{TRC,n}$ is the relative increase in the net rate to the product of interest with decreasing standard-state free energy of intermediate *n* while holding standard-state free energy of all other intermediates, all reactants, all products, and all transition states constant. $X_{RC,i,P}$ and $X_{RC,i,R}$ are the degrees of rate control of species *i* for producing product *P* and consuming reactant *R*, respectively. Finally, the value of $X_{SC,i}$ describes the relative increase in net selectivity to product *P* from reactant *R* due to the differential stabilization of the standard-state free energy for species *i*, which is either a transition

state or stable adsorbed intermediate state, holding all other species' energies constant. No assumptions were made regarding the rate-controlling steps in building our models.

3. RESULTS AND DISCUSSION

Figure 1 illustrates the reaction network investigated for the HDO of propanoic acid over a Cu(111) surface. The reaction network contains all elementary reaction steps that were previously considered in our prior studies for the decarbonylation and decarboxylation of propanoic acid to produce alkenes and alkanes on various transition metal surfaces.[25-31] In addition, reaction pathways for propanol and propionaldehyde production are considered in the reaction network based on our prior study of the HDO of PAc on Pt(111) surface.[32] The conversion of PAc (a dioxy species) to propanol or propionaldehyde (a monoxy species) must, at minimum, involve one C-O bond scission step followed by hydrogenation steps; although it is not obvious when that C-O bond scission occurs. Moreover, Cu catalysts have been shown to be effective catalysts for hydrogenation processes. We therefore considered hydrogenation of PAc prior to the first C-O bond scission, similar to the proposed reaction network for the hydrogenation of acetic acid to ethanol by Olcay et al.,[20] which eventually leads to the production of propanol and propionaldehyde (see Figure 1). We note that the reaction network is devoid of water-gas shift pathways that can reduce the CO partial pressure in the reactor. These pathways have been neglected since the active site for the water-gas shift rection is often found to be at the interface of a metal and oxide support,[74-77] i.e., it is not the metal surface itself. Thus, simulations must be performed at characteristic CO partial pressures. We found that the CO partial pressure does not have a significant impact on our microkinetic modeling results (see Table S8 of Supporting Information). In addition, we find adsorption of H_2 over Cu(111) to be quite different than over noble metal surfaces studied earlier.[25-30, 32] Instead of direct dissociation without any barrier over the noble metals, molecular H_2 first adsorbs on the Cu(111) catalyst surface with a ZPE corrected reaction energy of -0.20 eV, and then dissociates on the Cu(111) surface through a ZPE corrected activation energy barrier of 0.36 eV. Corresponding reaction and activation free energies for H_2 adsorption (step 89) and dissociation (step 48) can be found from Table 1.

In the following sections, we will first explore the DFT results for the HDO of PAc under gas phase conditions on a Cu(111) surface. Next, we will investigate the solvent effects on the adsorption strength of various surface species and elementary reaction steps. Then, we will explore

the results from our microkinetic reactor model, including the TOFs, product selectivity, rate-controlling steps, and the dominant reaction pathways for various products under various reaction conditions. Finally, reaction orders and apparent activation energies under both gas and liquid phase conditions will be computed.

3.1. Results from density functional theory calculations under gas phase condition

The reaction network investigated in this study starts with direct consumption of PAc through five main reactions as can be found from Figure 1. In the first reaction, the C-OH bond of PAc dissociates to propanoyl (CH_3CH_2CO) in step 1, which can undergo DCN followed by hydrogenation to C2 hydrocarbon products. In the second reaction, dehydrogenation of α-carbon of PAc to $CH_3CHCOOH$ takes place in step 2, which can produce C2 hydrocarbons through both DCN and DCX mechanisms. O-H bond dissociation of PAc to propionate (CH_3CH_2COO) occurs through a third reaction in step 28, which produces C2 products through a DCX mechanism. And finally, initial hydrogenation at the carbonyl oxygen to produce a diol species CH_3CH_2COHOH in step 49 (fourth reaction) and at the carbonyl carbon to CH_3CH_2CHOHO in step 50 (fifth reaction). The intermediates formed from the last two reactions, i.e., from initial hydrogenation of PAc (in step 49 and step 50), eventually produce propanol and propionaldehyde through C-OH dissociation followed by hydrogenation. From Figure 1 it is evident that although the DCN, DCX, propanol, and propionaldehyde production mechanisms are interconnected, key steps in each mechanism are distinguishable. For example, key steps to the DCX mechanism are O-H cleavage of PAc and its derivatives (CH_xCH_yCOOH, where x = 1,2,3 and y = 0,1,2) to form CH_xCH_yCOO intermediates followed by C-COO bond dissociation. In addition, DCX can also undergo C-COOH cleavage to form CH_xCH_y and COOH on the surface. Similarly, in key steps of the DCN mechanism, C-OH bond dissociations produce CH_xCH_yCO intermediates which form C2 hydrocarbons and CO after C-CO bond dissociation. The key steps of propanol and propionaldehyde production are the initial hydrogenation either at the carbonyl carbon or oxygen followed by a C-OH bond dissociation. In addition, hydrogenation of the intermediates formed after C-OH cleavage of the DCN mechanism can also produce propionaldehyde and eventually propanol. Table 1 illustrates the reaction and activation free energies for all elementary reaction steps involved in the reaction network at 573 K. A reaction temperature of 573 K was selected for this section since under vapor phase reaction conditions Cu catalysts were experimentally reported to be active at this temperature for the HDO of PAc.[24] For ease of understanding of DFT calculated results for the key steps of above mentioned

reaction mechanisms, we classified them into different classes of similar type of bond dissociations.

3.1.1. DCN mechanism

Class I: *C-OH bond dissociation*: The direct decomposition DCN pathway starts with -OH removal of PAc to produce CH_3CH_2CO and OH surface intermediates in step 1. The reaction is endothermic by 0.69 eV. The reaction has an activation free energy barrier of 1.41 eV. In the transition state, the carbonyl carbon and the hydroxyl O bind to two different Cu surface atoms with a 0.71 Å longer C-OH bond (2.09 Å) than that in PAc (1.38 Å). The -OH removal from dehydrogenated derivatives of PAc also shows a similar reaction nature. The dissociation of $CH_2CHCOOH$ to CH_2CHCO and OH surface intermediates in step 11 is endothermic by 0.67 eV. The reaction has an activation free energy barrier of 1.32 eV. The C-O bond length of the TS is enlarged to 2.28 Å.

Class II: *C-CO bond cleavage to produce CO*: The dehydroxylated intermediate of PAc after initial -OH removal to CH_3CH_2CO can undergo a direct decomposition DCN pathway to produce CH_3CH_2 and CO surface intermediates in step 3. The reaction is slightly endergonic with a reaction free energy as low as 0.09 eV. The reaction has a free energy barrier of 1.04 eV. In the transition state CH_3CH_2 binds to a Cu atop site, while CO binds at the hollow site. The C-C bond enlarges from 1.51 Å to 2.06 Å in the TS. Whereas the C-C bond breaking from deep dehydrogenated carbonyl intermediates becomes mildly exergonic. For example, C-CO bond cleavage from CHCHCO in step 18 is rater facile with an activation barrier of 0.68 eV and a reaction free energy of -0.49 eV. The TS is characterized by an enlarged C-C bond of 1.83 Å.

3.1.2. DCX mechanism

Class III: *O-H bond dissociation*: The direct decomposition DCX pathway starts with O-H bond dissociation of PAc to CH_3CH_2COO in step 28. This reaction is rather facile with a mildly exergonic reaction free energy of -0.40 eV and an activation barrier as low as 0.39 eV. The transition state is characterized by the hydroxyl H binding to the surface with the O-H distance enlarged to 1.54 Å from 1.00 Å of the same in PAc. However, O-H bond cleavage from dehydrogenated derivatives of PAc seems to become endergonic with a higher barrier. For example, O-H bond breaking from CH_3CCOOH in step 35 is mildly endergonic with a 0.48 eV reaction free energy and has a high activation barrier of 1.49 eV. In the TS, the O-H bond is elongated to 1.47 Å.

Class IV: *C-COO bond dissociation to produce CO_2*: The intermediate produced from hydroxyl H removal of PAc through direct DCX decomposition pathway can undergo C-COO cleavage to produce C2 hydrocarbons and CO_2 in step 29. This reaction is endergonic by 1.03 eV and has a high activation free energy barrier of 1.97 eV. The TS has an enlarged C-C distance of 2.08 Å (from 1.52 Å). Similar bond dissociations from α-carbon dehydrogenated intermediates have a somewhat lower activation barrier. For example, C-COO cleavage from CH_3CHCOO in step 33 is mildly endergonic with reaction free energy of 0.36 eV and an activation barrier of 1.06 eV. The TS has a C-C distance of 2.3 Å. The C-COO bond dissociation even becomes exergonic from the deep dehydrogenated intermediate CH_3CCOO in step 38 with reaction free energy -0.32 eV and has an activation barrier as low as 0.66 eV. The C-C bond distance in the TS is 2.17 Å.

Class V: *C-COOH bond dissociation*: Direct C-COOH scissions from CH_xCH_yCOOH intermediates seem to have high activation barriers. For example, C-COOH cleavage from $CH_3CHCOOH$ in step 32 is highly endergonic with reaction free energy of 1.22 eV and a high activation barrier of 1.68 eV. In the TS, the C-COO distance is 2.22 Å, which is elongated by 0.78 Å.

3.1.3. Propionaldehyde and propanol production mechanism

Class VI: *Initial hydrogenation of PAc*: Direct propionaldehyde and propanol formation pathways can start with initial hydrogenation either at the carbonyl carbon and/or carbonyl oxygen of PAc. Hydrogenation at carbonyl oxygen of PAc to a diol species CH_3CH_2COHOH in step 49 is highly endergonic and has an activation barrier of 1.29 eV. The TS of the reaction is characterized by an O-H distance of 1.17 Å. On the other hand, hydrogenation at a carbonyl carbon is relatively less energy demanding. Hydrogenation of PAc to CH_3CH_2CHOHO in step 50 is mildly endergonic by 0.44 eV with an activation energy of 1.02 eV. The C-H bond distance in the TS is 1.60 Å.

Class VII: *C-OH dissociation from initially hydrogenated intermediates*: -OH removal from the intermediate after initial hydrogenation at the carbonyl carbon of PAc in step 56 can directly produce propionaldehyde. This reaction is slightly endergonic by 0.10 eV and has a low activation barrier of 0.47 eV. The C-O bond distance in the TS is 2.00 Å. Whereas, -OH removal from the diol species after initial hydrogenation at the carbonyl oxygen of PAc in step 64 is endergonic by 0.67 eV. The activation barrier of step 64 is 1.64 eV. The TS is characterized by a C-O bond distance of 2.55 Å.

Class VIII: *hydrogenation of intermediates of the DCN mechanism to produce propionaldehyde*: This class of elementary steps seems rather facile. Hydrogenation of CH_3CH_2CO, formed after -OH removal of PAc through the DCN mechanism can also produce propionaldehyde in step 51. This reaction is exergonic by -0.15 eV and has a low activation barrier of 0.49 eV. In the TS, the C-H bond is 1.58 Å. Similarly, hydrogenation of CH_3CHCHO to propionaldehyde in step 68 is mildly exergonic by -0.10 eV and has a low activation barrier of 0.57 eV. The C-H bond distance in the TS is 1.68 Å.

Overall, it is difficult to identify the dominant reaction mechanism and the rate limiting elementary steps for the HDO of PAc over Cu(111) from only the activation barrier and reaction free energies under relevant reaction conditions. Thus, we developed a microkinetic model based on the DFT results and harmonic transition state theory, which will be discussed in section 3.3.

3.2. Effects of solvation

3.2.1. Solvent effect on the adsorption strength of surface species

The stability of a surface intermediate can be influenced by the presence of solvents. In general, the effect of solvents on the adsorption strength of a surface intermediate is related to the strength of solvent-adsorbate interaction relative to solvent-solvent interactions in solution, such as through hydrogen bonding in an aqueous phase. Depending on the nature of the solvent and adsorbate, certain types of cleavages can be facilitated or hindered in the solution phase with respect to the gas phase. Therefore, understanding the impact of the solvent environment on each individual surface intermediate can provide insight into how a solvent could affect and reshape the reaction mechanism.

To quantify the effects of the presence of a solvent on the adsorption strength of the surface intermediates, we computed the adsorption free energy in the absence and presence of a solvent as,

$$\mathrm{A\ (g) + *\ (g) \leftrightarrow A^*\ (g)} \tag{17}$$

$$\mathrm{A\ (l) + *\ (l) \leftrightarrow A^*\ (l)} \tag{18}$$

$$\Delta\Delta G_{solv} = \Delta G_{ads,A}(l) - \Delta G_{ads,A}(g)$$
$$= [G^{A*}(l) - G^{A*}(g)] - [G^{*}(l) - G^{*}(g)] \tag{19}$$

where $\Delta\Delta G_{solv}$ indicates the difference in the adsorption free energy of the corresponding intermediate in the presence and the absence of the solvent, $\Delta G_{ads,A}(l)$ and $\Delta G_{ads,A}(g)$ are the free

energies of a gas molecule A in the presence and absence of solvent, respectively, and $G^*(l)$ and $G^*(g)$ are the free energies of the free surface in the presence and absence of solvent, respectively.

The change in the adsorption free energies of the surface intermediates in the presence and the absence of the solvent has been calculated using the iSMS method at a temperature of 573 K and is tabulated in Table 2. One can notice from equation (19) that the negative value of $\Delta\Delta G_{solv}$ for an adsorbed intermediate indicates an increase in stabilization in the presence of a solvent, while a positive value of $\Delta\Delta G_{solv}$ for an adsorbed intermediate indicates a decrease in stabilization in the presence of a solvent. In water, the most stabilized intermediates are CH_3CCOO and CH_3CHCOO, due to the presence of a charged carboxyl group somewhat pointing in the direction of the solvent. In the presence of water as the solvent, their adsorption strengths are increased by 0.32 and 0.21 eV, respectively. The strong electrostatic interaction of the negatively charged carboxyl species with the solvent water molecules accounts for the stabilization of the adsorbed CH_3CCOO and CH_3CHCOO in the aqueous phase. In 1,4-dioxane, the change in adsorption strengths was reduced with a lower stabilization of 0.13 eV for CH_3CCOO and 0.11 eV for CH_3CHCOO. Such reduced stabilization in 1,4-dioxane is ascribed to the non-polar nature of the solvent that is incapable of strong interactions with the charged carboxyl group. In addition, the adsorption strength of the intermediates that have one or more -OH groups pointing in the direction of the solvent increases in the presence of the solvent. For example, an aqueous phase stabilizes the adsorption of $CH_3CHCOOH$ by 0.19 eV, COOH by 0.19 eV, $CH_3CHCHOHOH$ by 0.18 eV, CH_3CHCOH by 0.15 eV, and $CH_3CHCOHOH$ by 0.12 eV. Such increased stabilization in the aqueous phase is ascribed to the hydrogen-bonding interactions between the -OH group(s) of the adsorbed intermediate and solvent water molecules.

3.2.2. Solvent effect on elementary surface reactions

The solvent environment can play an important role in altering a reaction pathway and hence can reshape the overall reaction mechanism by affecting the stability of involved surface intermediates and transition states. Therefore, in this subsection, we discuss solvation effects of liquid water and 1,4-dioxane on elementary steps as the change in reaction $\left(\Delta\Delta G_{solv}^{rxn} = \Delta G_{solvent,i}^{rxn} - \Delta G_{gas,i}^{rxn}\right)$ and activation free energies $\left(\Delta\Delta G_{solv}^{\ddagger} = \Delta G_{solvent,i}^{\ddagger} - \Delta G_{gas,i}^{\ddagger}\right)$ relative to these values in the gas phase. The calculated $\Delta\Delta G_{solv}^{rxn}$ and $\Delta\Delta G_{solv}^{\ddagger}$ of all elementary steps in liquid water and 1,4-dioxane are computed at 573 K using our iSMS method and tabulated in Table 1, along with the corresponding gas phase reaction and activation free energies. From Table 1 one

notices that solvation has only a small effect on the adsorption of gas phase species on the Cu(111) surface and a larger effect on the reaction and activation free energies for surface reaction steps. For most of the surface reactions, we observe changes in free energy of approximately 0.20 eV. For example, for the dehydroxylation of surface adsorbed CH_3CH_2COOH in water, as described as step 1 in Table 1, the reaction free energy and activation free energy barrier decreased by 0.10 eV and 0.22 eV, respectively. The change in reaction free energy of this elementary reaction can be explained by the solvent effect on the adsorption strength of the surface intermediates involved as the reactant and products from the $\Delta\Delta G_{solv}$ values tabulated in Table 2. As described in Table 2, the $\Delta\Delta G_{solv}$ value for the products of step 1 is -0.05 eV for CH_3CH_2CO and -0.05 eV for OH, while the same for reactant CH_3CH_2COOH is 0.01 eV and hence, the overall reaction free energy of step 1 in Table 1 becomes 0.10 eV. However, for some of the surface reactions, we observe large deviations in reaction free energies due to solvation. For example, the reaction and activation free energies for decarboxylation of surface adsorbed CH_3CCOO, as shown in step 38 of Table 1, increased by 0.46 eV and 0.11 eV, respectively, in liquid water. Similarly, the reaction and activation free energies for decarboxylation of CH_3CHCOO increased by 0.36 eV and 0.11 eV, respectively, in liquid water as shown in step 33 of Table 1. These large solvent effects can be understood from the change in the exposure of the carboxylate group to the liquid phase,[32] and can also be explained by the $\Delta\Delta G_{solv}$ values of the involved surface intermediates, show in Table 2. In the reactant state, the somewhat charged carboxylate group points towards the solvent as the dehydrogenated carbon is strongly bound to the surface, and hence, a large $\Delta\Delta G_{solv}$ value of -0.32 eV for CH_3CCOO and -0.21 eV for CH_3CHCOO is found, while the product CO_2 is uncharged and has $\Delta\Delta G_{solv}$= 0.06 eV. Other product surface intermediates of step 38 and step 33, i.e., CH_3C and CH_3CH, respectively, also have a small positive $\Delta\Delta G_{solv}$ value of 0.09 eV each. The change in free energy in liquid 1,4-dioxane follows the same trend as in liquid water but is generally smaller.

In addition, the free energies calculated with $\pm$10% of the default COSMO Cu cavity show similar trends to those shown in Table 1 and are displayed in Table S1 and S2. However, it can be noticed from Table S1 that with a 10% increase in the default Cu cavity radius for the iSMS calculation the change in reaction and activation free energies of the elementary reactions slightly decreased. For example, the $\Delta\Delta G_{solv}^{rxn}$ and $\Delta\Delta G_{solv}^{\ddagger}$ values for step 33 in liquid water become 0.29 eV and 0.09 eV, respectively, with 10% increase in the default Cu cavity radius from 0.36 eV and

0.11 eV, respectively. While Table S2 shows that with a 10% decrease in the default Cu cavity radius for the iSMS calculation the change in reaction activation free energies of the elementary reactions slightly increased. For example, the $\Delta\Delta G_{solv}^{rxn}$ and $\Delta\Delta G_{solv}^{\ddagger}$ values for step 33 in liquid water become 0.41 eV and 0.13 eV, respectively, with a 10% decrease in the default Cu cavity radius. Such a slight increase in free energy changes with a decrease of cavity radius is expected due to an increase in solvent-adsorbate interaction. The calculated liquid phase free energies are not very sensitive to Cu cavity radius as slight changes of $\Delta\Delta G_{solv}^{rxn}$ and $\Delta\Delta G_{solv}^{\ddagger}$ with $\pm$10% change of the default COSMO Cu cavity does not change the overall predictions. In addition to the effects on free energies, a more detailed discussion on solvent effects on the observed kinetics is presented in the following sections.

3.3. Microkinetic Modelling Results

We developed a microkinetic model based on the reaction network shown in Figure 1 to predict the kinetic parameters for the HDO of PAc over Cu(111). The set of differential surface species equations was integrated using Matlab ODE solver ode15s until steady-state for two different temperatures of 473 and 573 K and fluid phase fugacities of 1 bar for propanoic acid, 0.1 bar for hydrogen, and zero for all other product molecules except CO, replicating low conversion conditions. As mentioned earlier, even small amounts of CO can affect simulation results (particularly on noble metal surfaces that bind CO strongly) and we studied the effect of CO fugacity in the range of 0.001 bar to 10 bar on the TOF (see Table S8 of Supporting Information). Fortunately, we did not find any significant impact of CO fugacity on the activity, product selectivity, or any other kinetic parameters such that we set the CO fugacity in the following to 0.001 bar. Also, solvent fugacities of water and 1,4-dioxane were found not to affect our results given the positive adsorption free energy of these solvents (see Table 1) and solvent fugacities of 47.5 bar and 17.9 bar (computed with COSMOtherm) for water and 1,4-dioxane at 573 K, respectively.

3.3.1. Activity and product selectivity

The TOFs obtained from the microkinetic analysis of the overall reaction network at different temperatures under both gas and liquid phase reaction conditions are summarized in Table 3. Corresponding surface coverages of the most abundant intermediates are also tabulated in Table 3. Unlike Group VIII metal surfaces, over Cu(111) adsorbed H* and CO* are not abundant

surface species. Instead, the Cu(111) surface remains mainly free of adsorbates (free site coverage above 80%) and only the carboxylate species, CH_3CH_2COO**, occupies some amount of surface sites at 573 K during the HDO of PAc. Given the high free site coverage and that lateral surface interactions approximately scale linearly with occupied surface coverage, we have not considered lateral interactions in the present work.

Under gas phase reaction conditions, the microkinetic model predicts that the reaction has a very low TOF of 6.7×10^{-9} s^{-1} at 473 K, which increases by three orders of magnitude to 8.1×10^{-6} s^{-1} at 573 K. This result agrees with the experimental findings of Lugo-José,[24] who did not report any vapor phase HDO activity of PAc over Cu catalysts at 200 °C and only a low activity at 300 °C. Under liquid phase reaction conditions, the TOF is increased by one order of magnitude relative to the gas phase at each temperature. This effect is more pronounced in the presence of liquid water relative to 1,4-dioxane. For example, at 573 K the TOF (gas phase: 8.1×10^{-6} s^{-1}) increases to 3.2×10^{-5} s^{-1} in liquid 1,4-dioxane and 9.0×10^{-5} s^{-1} in liquid water. The increase in activity in the liquid phase can be attributed to the change in the stabilization of rate-controlling steps as will be discussed in detail in section 3.3.3.1. Thus, solvents can significantly affect the reaction kinetics of the HDO of PAc over Cu(111). In addition to the conversion rate of PAc, solvents can also affect the product selectivity. As shown in Table 4, the overall selectivity of the DCN, DCX, and propionaldehyde production pathways in the gas phase are predicted as 16%, 79%, and 5%, respectively. These observations on product selectivity are in general agreement with the experimental findings of Lugo-José[24] who at 300 °C observed a selectivity toward C2 and EtCHO of 83% and 16%, respectively, at a low conversion (1%). In the liquid phase, the selectivity towards DCX products increases. Our model predicts the selectivity of the DCN, DCX, and propionaldehyde production pathways in liquid water to be 3%, 94%, and 2%. In contrast, in 1,4-dioxane the selectivity of the DCX pathway increased from 79% to 85% in the gas phase. Table 4 illustrates that ±10% changes in default Cu cavity radius for iSMS calculations also provides a similar trend of product selectivity as the default cavity. For example, the product selectivity through the DCX mechanism remains around ~95% in liquid water with a ±10% change in the Cu cavity radius from the default radius. Thus, under both gas and liquid phase reaction conditions, we observe that over Cu(111), the DCX is the dominant reaction pathway. This observation disagrees with our prior findings of the dominant reaction pathway of the HDO of PAc over Pd(111),[25, 28] Pd(211),[26-27] Ru(0001),[30] Ni(111),[31] where we observed DCN pathways to be

preferred over DCX steps, and over Pt(111) and Rh(111),[32-33] where propanol and propionaldehyde are favored over DCN and DCX products.

3.3.2. Dominant reaction pathways

The calculated rates of all elementary reactions involved in the microkinetic model under gas phase reaction condition are shown in Figure 1. Figure 1 demonstrates that under gas phase conditions the adsorbed PAc mainly undergoes DCX pathways that start with a couple of dehydrogenation steps to produce $CH_3CHCOO***$ through two competitive pathways: pathways that start with dehydrogenation from carboxylic acid O-H in step 28, followed by α-carbon dehydrogenation step 30, and the reverse sequence of bond cleavages, i.e., α-carbon dehydrogenation in step 2, followed by carboxylic O-H cleavege in step 31. Decarboxylation following from $CH_3CHCOO***$ produces CH_3CH with a rate of 4.5×10^{-6} s^{-1} in step 33, which is followed by further dehydrogenation and hydrogenation steps to produce C_2H_2 as the major product. CH_3CH_2COO** produced from dehydrogenation of the carboxylic acid O-H of PAc also undergoes competitive decarboxylation to CH_3CH_2 (step 29) with a rate of 1.9×10^{-6} s^{-1}, which produces C_2H_4 through further dehydrogenation. Clearly, under gas phase conditions the DCX pathway, $CH_3CH_2COOH* \rightarrow CH_3CH_2COO** \rightarrow CH_3CHCOO*** \rightarrow CH_3CH** \rightarrow CH_2CH*** \rightarrow C_2H_2***$, is dominant as shown by bold dashed arrows in Figure 1. Dependent on the acetylene and ethylene partial pressure, these products can be hydrogenated to ethane. According to the rate shown in Figure 1, the DCN pathway and aldehyde formation can also occur but in much smaller rates than DCX. This also reflects the product selectivity shown in Table 4. The dominant DCN pathway starts with dihydroxylation of $CH_3CHCOOH***$ to $CH_3CHCO***$ (step 5) with a rate of 1.3×10^{-6} s^{-1}, followed by one α-carbon dehydrogenation to CH_3CCO** (step 9). Next, decarbonylation from CH_3CCO** produces CH_3C* (step 14) with a rate of 1.3×10^{-6} s^{-1}, which is followed by some dehydrogenation and hydrogenation processes to produce C_2H_2. All other DCN pathways have a much lower rate. In addition to the DCN pathways, a couple of hydrogenations at the carbonyl carbon and α-carbon of $CH_3CHCO***$ produce propionaldehyde through step 61 and step 68 with a low rate of 2.8×10^{-7} s^{-1}. Other pathways that can produce an aldehyde (step 50, 51 and 56) show significantly smaller rates. Moreover, all the other pathways that produce alcohol, ketone and esters have very low rates at small PAc conversion and hardly any of these products are observed.

Under the liquid phase reaction conditions, the reaction flux of the HDO of PAc over Cu(111) displays a similar characteristic to the vapor phase. Figure 2 and 3 illustrate the calculated rates of all elementary reactions involved in the microkinetic model in liquid water and 1,4-dioxane, respectively. The key solvent effect is an overall acceleration of the PAc conversion rate by one order of magnitude in liquid water due to an acceleration of DCX pathways. DCN and propionaldehyde pathways increase in liquid water by only approximately a factor of 2. Thus, the selectivity shifts in condensed phase further in the direction of the DCX products and 95% of the reaction flux proceeds through steps 33 and 29. However, the dominant reaction pathway remains unchanged relative to the gas phase, i.e., $CH_3CH_2COOH^* \rightarrow CH_3CH_2COO^{**} \rightarrow CH_3CHCOO^{***} \rightarrow CH_3CH^{**} \rightarrow CH_2CH^{***} \rightarrow C_2H_2^{***}$. In a liquid 1,4-dioxane reaction environment, we observe that the reaction flux of the HDO of PAc shows a similar characteristic to the vapor and condensed water phase. Solvent affects are smaller and the rate increases relative to the vapor phase are smaller such that approximately 85% of the reaction flux follows DCX pathways and the propionaldehyde selectivity is ~3%. In addition, the rates calculated with $\pm$10% of the default COSMO Cu cavity show similar trends as calculated with the default cavity under the corresponding liquid phase, which can be seen in Figure S1 to S4 of the supporting information. From Figure S1 to Figure S4 one can notice that the dominant reaction pathway remains unchanged with $\pm$10% change relative to the default Cu cavity radius both in liquid water and 1,4-dioxane as well as the gas phase condition, i.e., $CH_3CH_2COOH^* \rightarrow CH_3CH_2COO^{**} \rightarrow CH_3CHCOO^{***} \rightarrow CH_3CH^{**} \rightarrow CH_2CH^{***} \rightarrow C_2H_2^{***}$.

3.3.3. Sensitivity analysis

3.3.3.1. Degrees of rate control

From the discussion of section 3.3.2. it is clear that the HDO of PAc over Cu(111) mainly proceeds through the DCX mechanism, which is quite distinct from other noble metal catalyst surfaces that primarily occur through DCN pathways.[25-28, 30, 32] In this section, we predict the rate-controlling steps for the HDO of PAc over a Cu(111) surface. Calculated degrees of rate control ($X_{RC,i}$) in various reaction environments are tabulated in Table 5.

Table 5 reveals that under gas phase reaction conditions, the C-COO bond dissociation of the DCX pathways, step 33 and step 29 (as described in Figure 1 and Table 1), have the largest

degrees of rate control of 0.26 and 0.24, respectively. Additionally, the dehydrogenation steps from the α-carbon in step 30 and step 2, and the O-H cleavage of $CH_3CHCOOH^{***}$ in step 31 are predicted to be partially rate-controlling with X_{RC} values of 0.16, 0.06, and 0.10, respectively. Finally, the C-OH bond dissociation step from $CH_3CHCOOH^{***}$ in step 5 is partially rate controlling with $X_{RC} = 0.14$.

In liquid water, the C-COO bond dissociation step 33 of the DCX pathway becomes the largest rate-controlling step with a X_{RC} value of 0.60. Another competitive C-COO bond dissociation step 29 is also partially rate-controlling with an X_{RC} value of 0.32. The dehydrogenations at step 30 and C-OH bond cleavage at step 5 display a very low degree of rate control of 0.02 each. It is worth noting that such a change in the degree of rate control in liquid water relative to the gas phase can be explained by the changes in the free energy barrier due to solvation. Table 1 shows that the free energy barrier of step 33 increases by 0.11 eV in the presence of liquid water. Also, the dehydrogenation barriers at step 30 and step 2 are diminished by 0.27 eV and 0.13 eV, respectively, in liquid water. Although the C-OH bond dissociation barrier at step 5 increases in water by 0.16 eV, DCX pathways are the main reaction flux and indeed, step 5 becomes less rate controlling. It is worth mentioning that in the presence of water, H_3O^* and OH* species could be potential hydrogenating species in addition to the here considered surface H* species as observed in recent related studies.[78-80] However, in the present study, we found that under all liquid water reaction conditions hydrogenation steps are not rate limiting, rather, the C-COO bond dissociation in step 33 and in step 29 of the DCX pathway are the rate limiting steps (see Table 5). Thus, any potential hydrogenation by surface adsorbed H_3O^* and OH* species will not affect the kinetics of the HDO of PAc over a Cu(111) catalyst under liquid water conditions. Similarly, in liquid 1,4-dioxane step 33 and step 29 of the DCX pathway show the largest rate control with X_{RC} values of 0.46 and 0.26, respectively.

Given that the Cu(111) surface remains mostly free of adsorbates during the HDO of PAc at 573 K, and that $CH_3CH_2COO^{**}$ is the only adsorbate with significant surface coverage, $CH_3CH_2COO^{**}$ is the only species with signficant degree of thermodynamic rate control (X_{TRC}). Table 6 illustrates thermodynamic rate control values for $CH_3CH_2COO^{**}$ under both gas phase and liquid phase conditions between -0.19 and -0.47. Thus, destabilizing the adsorption of $CH_3CH_2COO^{**}$ facilitates the HDO of PAc over Cu(111) under all reaction conditions.

3.3.3.2. Degrees of selectivity control

Table 7 show the degrees of selectivity control of various DCN, DCX, and propionaldehyde production steps under vapor phase reaction conditions. Accelerating the C-OH bond cleavage of step 5 increases the selectivity towards DCN and propionaldehyde production while reducing the selectivity towards DCX pathways. Additionally, stabilizations of the C-H bond cleavage transition states of steps 2 and 7 slightly increase the selectivity towards DCN products. Moreover, we observed a pattern in the degrees of selectivity control. Stabilization of the transition state of the reaction steps, which are involved in the DCN mechanism (step 8, 9, and14), increase the DCN product selectivity, while they decrease the selectivity of the competitive propionaldehyde production. In contrast, acceleration of propionaldehyde production reaction steps (step 50, 56, 61, and 68) increase the selectivity to propionaldehyde by diminishing the competitive DCN pathways. In comparison, stabilizing critical transition states in the DCX mechanism (step 29, 30, 31, and 33) increase the selectivity towards DCX products while decreasing the selectivity to both DCN pathways and propionaldehyde production. The reason for this selectivity behavior originates from both DCN pathways and propionaldehyde production having the difficult C-OH bond cleavage in common that is not present in the DCX pathways.

Under liquid phase conditions (see Table 8 and 9), the degrees of selectivity control follow the same trend as in the vapor phase, i.e., stabilizing the transition states of key DCX steps increases the DCX selectivity while concurrently decreasing the selectivity of both DCN steps and propionaldehyde production. In liquid 1,4-dioxane, the acceleration of steps 2, 5, and 7 increases the selectivity of the DCN pathways and propionaldehyde production most, while the selectivity of DCX pathways is diminished. Additionally, the stabilization of the transition state of the DCN steps 8, 9, and 14 increases the DCN pathway selectivity while decreasing the competitive propionaldehyde selectivity. In contrast, acceleration of reaction steps 1, 68, and 50 mainly improves the propionaldehyde selectivity while slightly diminishing the DCN and DCX product selectivity. However, stabilizing the transition state of the DCX steps 29 and 33 decreases the selectivity of both DCN and propionaldehyde production while improving the DCX product selectivity.

Similarly, for liquid water, Table 9 shows that acceleration of DCX reaction steps 29 and 33 increases the DCX product selectivity while mostly decreasing the DCN and propionaldehyde

production in liquid water. Stabilization of the transition state of steps 5 and 7 mostly increases DCN product selectivity along with a decrease in the DCX pathways. Also, stabilizing the transition state of step 1 mostly increases the selectivity of propionaldehyde while the DCX product pathway selectivity decreases. In liquid water, increasing the selectivity towards propionaldehyde requires accelerating the C-OH bond cleavage while facilitating hydrogenation reactions. In contrast, facilitating production of alkanes requires acceleration of C-H bond cleavage reactions.

Finally, the thermodynamic selectivity control of $CH_3CH_2COO^{**}$ under both gas and liquid phase reaction conditions is tabulated in Table 10 and further stabilization of adsorbed $CH_3CH_2COO^{**}$ increases the selectivity towards DCX pathways while it decreases the DCN and propionaldehyde production pathways.

3.3.3.3. Apparent activation barrier and reaction orders

In order to understand the sensitivity of our modeling results with regard to temparature, Figure 4 illustrates the apparent activation energy (E_{app}) within a temperature range of 473 K to 573 K under vapor and liquid phase conditions. Our model predicts large apparent activation barriers of 1.7 eV, 1.8 eV, and 1.9 eV in vapor, liquid 1,4-dioxane, and liquid water, respectively. Unfortunately, there are no reported experimental apparent activation barriers available for the HDO of PAc over Cu catalysts.

To understand the sensitivity of our model towards the fluid phase fugacities in the reaction system, we have calculated the reaction orders of PAc and H_2 at 573 K. Figure 5(a) illustrates the reaction order for PAc in vapor, liquid water, and liquid 1,4-dioxane as 0.82, 0.63 and 0.65, respectively. Thus, a near first-order dependence on the PAc fugacity is observed. The reaction order for H_2, shown in Figure 5(b), is -0.49, -0.60 and -0.54 in vapor, liquid water, and liquid 1,4-dioxane, respectively. Such negative half-order dependence on H_2 is interesting given that H* is not a dominant surface species during the HDO of PAc over Cu(111), unlike Group VIII metal surfaces. However, the observed negative H_2 reaction order can be explained from the dominant reaction flux and rate-limiting step of the HDO of PAc over Cu(111). In section 3.2.3.1., we noted that the DCX mechanism is the dominant reaction pathway and C-COO bond dissociation is the rate controlling step. In addition, the dehydrogenation steps 2, 30, and 31 are also partially rate controlling. If we would consider the C-COO bond dissociation (step 29: $CH_3CH_2COO^{**} \rightarrow$

CH_3CH_2* + CO_2*) to be the sole irreversible, rate controlling step, then the rate equation would be $r_{29} = k_{29}\ \theta_{CH3CH2COO**}$. If now PAc adsorption and the dehydrogenation step 28 are in equilibrium, i.e., CH_3CH_2COOH (gas) + 2* ⇌ CH_3CH_2COO** + $\frac{1}{2}$ H_2 (gas), then $\theta_{CH3CH2COO**}$ can be computed from K = $\frac{\theta_{CH3CH2COO**}\ P_{H2}^{0.5}}{P_{CH3CH2COOH}\ \theta_*^2}$ and the rate equation for consumption of PAc would become $r_{29} = \frac{k_{29}K P_{CH3CH2COOH}\ \theta_*^2}{P_{H2}^{0.5}}$, where $P_{CH3CH2COOH}$ is the partial pressure/fugacity of PAc and θ* ≈ 1 (see Table 3), explaining the observed negative half -order dependency on H_2.

3.3.4. Effect of high H_2 partial pressure on the reaction kinetics

So far, discussions have centered around a moderate to low H_2 partial pressures. However, the HDO reaction often occurs at elevated pressures of H_2 such as 10 bar. Figure S9 of the Supporting Information illustrates calculated rates of all elementary reactions included in the microkinetic model under gas phase reaction conditions. For simplicity, only those steps which have noteworthy values are shown in Figure S9. At 10 bar H_2 partial pressure, the selectivity changes significantly and the dominant reaction flux shifts towards hydrogenation at the carbonyl carbon of PAc to produce CH_3CH_2CHOHO* (step 50: CH_3CH_2COOH* + H* → CH_3CH_2CHOHO*), followed by C-OH bond dissociation (step 56: CH_3CH_2CHOHO* + * → CH_3CH_2CHO* + OH*) to produce propionaldehyde (CH_3CH_2CHO) as the major product. Thus, the product selectivity changes to 78% propionaldehyde and only 22% to DCX and DCN products. Interestingly, the TOF is only slightly diminished to 1.5×10^{-6} s^{-1} relative to the low H_2 partial pressure scenario of 0.1 bar. The hydrogenation step 50 is rate-controlling under these conditions with an X_{RC} value of 0.56. It is worth mentioning that the partial pressures of all product species were set to zero in the simulations described above in a low conversion model. In order to confirm whether larger amounts of propionaldehyde could be produced at higher H_2 pressures, we set the propionaldehyde fugacity to 0.001 bar, which is less than 1% conversion of PAc.[24] The calculated rates of the elementary reactions are shown in Figure S10 of supporting information. Figure S10 demonstrates that while the dominant reaction pathway remains the same for producing adsorbed CH_3CH_2CHO*, the majority of CH_3CH_2CHO* can undergo "rapid" decarbonylation to C2 products and only small amounts of propionaldehyde are produced. By omitting the desorption step of CH_3CH_2CHO* from the microkinetic model (equilibrium between adsorbed and fluid phase propionaldehyde i.e. CH_3CH_2CHO + * ⇌ CH_3CH_2CHO*, where equilibrium constant of

this elementary process (K) = 8.0×10^{-9} with surface coverage of adsorbed $CH_3CH_2CHO^*$, $\theta_{CH3CH2CHO^*} = 1.22\times10^{-22}$, while free Cu(111) surface, $\theta^* = 9.84\times10^{-1}$, at 573 K and 10 bar H_2 partial pressure), we can compute the maximum amount of propionaldehyde produced is only 1.42×10^{-14} bar. This essentially means that the $CH_3CH_2CHO^*$ generated in the reaction mixture at 573 K and 10 bar H_2 partial pressure will undergo complete decomposition. Figure S11 of the Supporting Information illustrates the reaction flux under these conditions, highlighting that at higher H_2 partial pressures the decarbonylation products are produced from the re-adsorption of propionaldehyde generated in the reaction mixture and eventually, the dominant HDO mechanism of PAc over Cu(111) becomes a DCN mechanism, which is fundamentally different to the low H_2 partial pressure scenario.

4. CONCLUSIONS

In the present work, microkinetic models based on harmonic transition state theory and density functional theory calculations were developed to systematically explore the hydrodeoxygenation (HDO) of propanoic acid (PAc) over Cu(111) under both gas and liquid phase conditions. Under all the reaction conditions considered and unlike other Group VIII noble metal surfaces, Cu(111) is hardly covered by any surface species and displays no dependence on the CO partial pressure at 573 K, due to the lower CO adsorption energy on Cu. This characteristic is unique for Cu and opens a scope to design an active catalyst for the HDO of PAc through suitable alloy formation with more active Group VIII metals. Overall, we observed a low rate at 573 K for the HDO of PAc over Cu(111) under gas phase reaction conditions, which is in line with previous experimental observations. However, the TOFs seem to increase considerably in the presence of solvents. At 573 K and in liquid 1,4-dioxane, the TOF for the HDO of PAc is predicted to increase by factors of four, whereas, in liquid water, the TOF increases by one order of magnitude. Unlike Group VIII metal surfaces, decarboxylation (DCX) is the dominant reaction flux for the HDO of PAc over Cu(111) under both gas and liquid phase reaction conditions at low hydrogen partial pressure of 0.1 bar. Under these conditions, the dominant reaction pathway is $CH_3CH_2COOH^* \rightarrow CH_3CH_2COO^{**} \rightarrow CH_3CHCOO^{***} \rightarrow CH_3CH^{**} \rightarrow CH_2CH^{***} \rightarrow C_2H_2^{***}$. Here, the C-COO bond dissociation is the rate-controlling elementary step, which is quite distinct from the rate-controlling C-OH bond dissociation step observed for Group VIII metal surfaces for the same

reaction. Indeed, DCX products are observed as the major products with only minor production of decarbonylation (DCN) products and propionaldehyde. However, selectivity control analysis shows that the selectivity of the DCN and propionaldehyde can be increased by stabilizing the transition states involved in the DCN and propionaldehyde production mechanism with the smaller formation of DCX products and vice versa. We observed high apparent activation energies under all reaction conditions and a near first-order dependence on PAc and a negative half-order dependence on the hydrogen partial pressure. Interestingly, at high hydrogen partial pressures of 10 bar, we observed a shift in the reaction mechanism and product selectivity. At such high hydrogen partial pressures, propionaldehyde production pathways are the dominant reaction flux, with hydrogenation at the carbonyl carbon of PAc as the rate-controlling elementary reaction step and propionaldehyde as the major product. We speculate that at high hydrogen partial pressure the HDO of PAc over Cu(111) first produces propionaldehyde, which re-adsorbs and reacts further through the DCN mechanism to produce C2 products. This mechanistic understanding of the HDO of PAc over Cu(111) encourages further studies of suitable Cu alloy catalysts with the goal of tuning the adsorption strength of hydrocarbon and adsorbed hydrogen species to generate a highly active catalysts for the HDO of organic acids.

Supporting Information

Reaction and activation free energies of all elementary reaction steps in the presence of liquid water and 1,4-dioxane using a 10% increased (Table S1) and 10% decreased (Table S2) COSMO Cu cavity radius in the solvation calculations, the number of surface species per surface metal atom under both gas and liquid phase reaction conditions (Table S3), Degree of selectivity control for reaction steps under liquid 1,4-dioxane reaction conditions using a 10% decreased (Table S4) and 10% increased (Table S5) COSMO Cu cavity radius in the solvation calculations, Degree of selectivity control for reaction steps under liquid water reaction conditions using a 10% decreased (Table S6) and 10% increased (Table S7) COSMO Cu cavity radius in the solvation calculations, TOFs (s^{-1}) and the number of surface species occupied per surface metal atom of the most abundant surface intermediates in the vapor phase over a Cu(111) surface at different CO fugacity (Table S8), TOFs (s^{-1}) of various elementary steps in the reaction network under liquid 1,4-dioxane reaction conditions using a 10% decreased (Figure S1) and 10% increased (Figure S2) COSMO

Cu cavity radius in the solvation calculations, TOFs (s^{-1}) of various elementary steps in the reaction network under liquid water reaction conditions using a 10% decreased (Figure S3) and 10% increased (Figure S4) COSMO Cu cavity radius in the solvation calculations, Arrhenius plot in the temperature range of 473-573 K in the presence of liquid water and 1,4-dioxane using a 10% decreased (Figure S5) and 10% increased (Figure S6) of the default COSMO Cu cavity radius in the solvation calculations, Reaction orders of Propanoic acid and H_2 in the presence of liquid water and 1,4-dioxane using a 10% decreased (Figure S7) and 10% increased (Figure S8) COSMO Cu cavity radius in the solvation calculations, TOFs (s^{-1}) of various elementary steps in the reaction network under vapor phase reaction conditions at a high hydrogen partial pressure/fugacity of 10 bar (Figure S9), TOFs (s^{-1}) of various elementary steps in the reaction network under vapor phase reaction conditions at a high hydrogen partial pressure/fugacity of 10 bar and a very small partial pressure/fugacity of propionaldehyde of 0.001 bar (Figure S10), TOFs (s^{-1}) of various elementary steps in the reaction network under vapor phase reaction conditions at a high hydrogen partial pressure/fugacity of 10 bar and omitting propionaldehyde desorption step from the microkinetic model (Figure S11)

Acknowledgments

This work was supported by the U.S. Department of Energy, Office of Basic Energy Sciences, Catalysis Science program under contract DE-SC0007167. Initial gas phase calculations were partially supported by the National Science Foundation under award number DMREF-1534260. C.F. acknowledges financial support from the National Science Foundation under award number DGE-1250052. This work was also supported by the South Carolina State Center for Strategic Approaches to the Generation of Electricity (SAGE). Computing resources from the National Energy Research Scientific Computing Center (NERSC) under Contract No. DE-AC02-05CH11231, XSEDE resources provided by the San Diego Supercomputer Center (SDSC) and Texas Advanced Computing Center (TACC) under grant number TG-CTS090100, Pacific Northwest National Laboratory (Ringgold ID 130367, Grant Proposals 51163 and 51711) and the University of South Carolina's High Performance Computing Group are gratefully acknowledged.

REFERENCES:

1. Bessou, C.; Ferchaud, F.; Gabrielle, B.; Mary, B., Biofuels, Greenhouse Gases and Climate Change. A Review. *Agron Sustain Dev* **2011**, *31*, 1-79.
2. Carpenter, D.; Westover, T. L.; Czernik, S.; Jablonski, W., Biomass Feedstocks for Renewable Fuel Production: A Review of the Impacts of Feedstock and Pretreatment on the Yield and Product Distribution of Fast Pyrolysis Bio-Oils and Vapors. *Green Chemistry* **2014**, *16*, 384-406.
3. Stöcker, M., Biofuels and Biomass-to-Liquid Fuels in the Biorefinery: Catalytic Conversion of Lignocellulosic Biomass Using Porous Materials. *Angewandte Chemie International Edition* **2008**, *47*, 9200-9211.
4. Regalbuto, J., An Nsf Perspective on Next Generation Hydrocarbon Biorefineries. *Computers & chemical engineering* **2010**, *34*, 1393-1396.
5. Knothe, G., Dependence of Biodiesel Fuel Properties on the Structure of Fatty Acid Alkyl Esters. *Fuel processing technology* **2005**, *86*, 1059-1070.
6. Pham, T. N.; Shi, D.; Resasco, D. E., Evaluating Strategies for Catalytic Upgrading of Pyrolysis Oil in Liquid Phase. *Applied Catalysis B: Environmental* **2014**, *145*, 10-23.
7. Ramos, M. J.; Fernández, C. M.; Casas, A.; Rodríguez, L.; Pérez, Á., Influence of Fatty Acid Composition of Raw Materials on Biodiesel Properties. *Bioresource technology* **2009**, *100*, 261-268.
8. Serrano-Ruiz, J. C.; Dumesic, J. A., Catalytic Routes for the Conversion of Biomass into Liquid Hydrocarbon Transportation Fuels. *Energy & Environmental Science* **2011**, *4*, 83-99.
9. Chheda, J. N.; Huber, G. W.; Dumesic, J. A., Liquid-Phase Catalytic Processing of Biomass-Derived Oxygenated Hydrocarbons to Fuels and Chemicals. *Angewandte Chemie International Edition* **2007**, *46*, 7164-7183.
10. Huber, G. W.; Iborra, S.; Corma, A., Synthesis of Transportation Fuels from Biomass: Chemistry, Catalysts, and Engineering. *Chemical reviews* **2006**, *106*, 4044-4098.
11. Kubička, D., Future Refining Catalysis-Introduction of Biomass Feedstocks. *Collection of Czechoslovak chemical communications* **2008**, *73*, 1015-1044.

12. Wang, J.; Zhang, X.; Sun, Q.; Chan, S.; Su, H., Chain Growth Mechanism on Bimetallic Surfaces for Higher Alcohol Synthesis from Syngas. *Catalysis Communications* **2015**, *61*, 57-61.
13. Alcala, R.; Shabaker, J. W.; Huber, G. W.; Sanchez-Castillo, M. A.; Dumesic, J. A., Experimental and Dft Studies of the Conversion of Ethanol and Acetic Acid on Ptsn-Based Catalysts. *The Journal of Physical Chemistry B* **2005**, *109*, 2074-2085.
14. Chen, L.; Li, Y.; Zhang, X.; Zhang, Q.; Wang, T.; Ma, L., Mechanistic Insights into the Effects of Support on the Reaction Pathway for Aqueous-Phase Hydrogenation of Carboxylic Acid over the Supported Ru Catalysts. *Applied Catalysis A: General* **2014**, *478*, 117-128.
15. Chen, L.; Zhu, Y.; Zheng, H.; Zhang, C.; Li, Y., Aqueous-Phase Hydrodeoxygenation of Propanoic Acid over the Ru/Zro2 and Ru–Mo/Zro2 Catalysts. *Applied Catalysis A: General* **2012**, *411*, 95-104.
16. Chen, Y.; Miller, D. J.; Jackson, J. E., Kinetics of Aqueous-Phase Hydrogenation of Organic Acids and Their Mixtures over Carbon Supported Ruthenium Catalyst. *Industrial & engineering chemistry research* **2007**, *46*, 3334-3340.
17. Gursahani, K. I.; Alcalá, R.; Cortright, R. D.; Dumesic, J. A., Reaction Kinetics Measurements and Analysis of Reaction Pathways for Conversions of Acetic Acid, Ethanol, and Ethyl Acetate over Silica-Supported Pt. *Applied Catalysis A: General* **2001**, *222*, 369-392.
18. He, Z.; Wang, X., Required Catalytic Properties for Alkane Production from Carboxylic Acids: Hydrodeoxygenation of Acetic Acid. *Journal of Energy Chemistry* **2013**, *22*, 883-894.
19. Lugo-José, Y. K.; Monnier, J. R.; Williams, C. T., Gas-Phase, Catalytic Hydrodeoxygenation of Propanoic Acid, over Supported Group Viii Noble Metals: Metal and Support Effects. *Applied Catalysis A: General* **2014**, *469*, 410-418.
20. Olcay, H.; Xu, L. J.; Xu, Y.; Huber, G. W., Aqueous-Phase Hydrogenation of Acetic Acid over Transition Metal Catalysts. *Chemcatchem* **2010**, *2*, 1420-1424.
21. Olcay, H.; Xu, Y.; Huber, G. W., Effects of Hydrogen and Water on the Activity and Selectivity of Acetic Acid Hydrogenation on Ruthenium. *Green Chemistry* **2014**, *16*, 911-924.
22. Rachmady, W.; Vannice, M. A., Acetic Acid Hydrogenation over Supported Platinum Catalysts. *Journal of catalysis* **2000**, *192*, 322-334.
23. Shangguan, J.; Olarte, M. V.; Chin, Y.-H. C., Mechanistic Insights on Co and Cc Bond Activation and Hydrogen Insertion During Acetic Acid Hydrogenation Catalyzed by Ruthenium Clusters in Aqueous Medium. *Journal of catalysis* **2016**, *340*, 107-121.
24. José, L.; Yuliana, K. Gas-Phase, Catalytic Hydrodeoxygenation of Propanoic Acid over Supported Group Viii Noble Metals. University of South Carolina, Columbia, 2014.
25. Behtash, S.; Lu, J.; Faheem, M.; Heyden, A., Solvent Effects on the Hydrodeoxygenation of Propanoic Acid over Pd (111) Model Surfaces. *Green Chemistry* **2014**, *16*, 605-616.
26. Behtash, S.; Lu, J.; Mamun, O.; Williams, C. T.; Monnier, J. R.; Heyden, A., Solvation Effects in the Hydrodeoxygenation of Propanoic Acid over a Model Pd (211) Catalyst. *The Journal of Physical Chemistry C* **2016**, *120*, 2724-2736.
27. Behtash, S.; Lu, J.; Williams, C. T.; Monnier, J. R.; Heyden, A., Effect of Palladium Surface Structure on the Hydrodeoxygenation of Propanoic Acid: Identification of Active Sites. *The Journal of Physical Chemistry C* **2015**, *119*, 1928-1942.
28. Lu, J.; Behtash, S.; Faheem, M.; Heyden, A., Microkinetic Modeling of the Decarboxylation and Decarbonylation of Propanoic Acid over Pd (1 1 1) Model Surfaces Based on Parameters Obtained from First Principles. *Journal of catalysis* **2013**, *305*, 56-66.
29. Lu, J.; Behtash, S.; Heyden, A., Theoretical Investigation of the Reaction Mechanism of the Decarboxylation and Decarbonylation of Propanoic Acid on Pd (111) Model Surfaces. *The Journal of Physical Chemistry C* **2012**, *116*, 14328-14341.

30. Lu, J.; Faheem, M.; Behtash, S.; Heyden, A., Theoretical Investigation of the Decarboxylation and Decarbonylation Mechanism of Propanoic Acid over a Ru (0 0 0 1) Model Surface. *Journal of catalysis* **2015**, *324*, 14-24.
31. Zare, M.; Solomon, R. V.; Yang, W.; Yonge, A.; Heyden, A., Theoretical Investigation of Solvent Effects on the Hydrodeoxygenation of Propionic Acid over a Ni (111) Catalyst Model. *The Journal of Physical Chemistry C* **2020**, *124*, 16488-16500.
32. Yang, W.; Solomon, R. V.; Lu, J.; Mamun, O.; Bond, J. Q.; Heyden, A., Unraveling the Mechanism of the Hydrodeoxygenation of Propionic Acid over a Pt (1 1 1) Surface in Vapor and Liquid Phases. *Journal of Catalysis* **2020**, *381*, 547-560.
33. Yang, W.; Solomon, R. V.; Mamun, O.; Bond, J. Q.; Heyden, A., Investigation of the Reaction Mechanism of the Hydrodeoxygenation of Propionic Acid over a Rh (1 1 1) Surface: A First Principles Study. *Journal of Catalysis* **2020**, *391*, 98-110.
34. Zhang, M.; Yao, R.; Jiang, H.; Li, G.; Chen, Y., Insights into the Mechanism of Acetic Acid Hydrogenation to Ethanol on Cu (111) Surface. *Applied Surface Science* **2017**, *412*, 342-349.
35. Zhang, M.; Yao, R.; Jiang, H.; Li, G.; Chen, Y., Catalytic Activity of Transition Metal Doped Cu (111) Surfaces for Ethanol Synthesis from Acetic Acid Hydrogenation: A Dft Study. *RSC advances* **2017**, *7*, 1443-1452.
36. Sun, X.; Zhang, R.; Wang, B., Insights into the Preference of Chx (X= 1–3) Formation from Co Hydrogenation on Cu (111) Surface. *Applied Surface Science* **2013**, *265*, 720-730.
37. Wang, J.; Kawazoe, Y.; Sun, Q.; Chan, S.; Su, H., The Selectivity and Activity of Catalyst for Co Hydrogenation to Methanol and Hydrocarbon: A Comparative Study on Cu, Co and Ni Surfaces. *Surface Science* **2016**, *645*, 30-40.
38. Xu, X.-C.; Su, J.; Tian, P.; Fu, D.; Dai, W.; Mao, W.; Yuan, W.-K.; Xu, J.; Han, Y.-F., First-Principles Study of C2 Oxygenates Synthesis Directly from Syngas over Cocu Bimetallic Catalysts. *The Journal of Physical Chemistry C* **2014**, *119*, 216-227.
39. Zhang, R.; Wang, G.; Wang, B., Insights into the Mechanism of Ethanol Formation from Syngas on Cu and an Expanded Prediction of Improved Cu-Based Catalyst. *Journal of catalysis* **2013**, *305*, 238-255.
40. Zheng, H.; Zhang, R.; Li, Z.; Wang, B., Insight into the Mechanism and Possibility of Ethanol Formation from Syngas on Cu (1 0 0) Surface. *Journal of Molecular Catalysis A: Chemical* **2015**, *404*, 115-130.
41. Grabow, L.; Mavrikakis, M., Mechanism of Methanol Synthesis on Cu through Co2 and Co Hydrogenation. *Acs Catalysis* **2011**, *1*, 365-384.
42. Yang, Y.; White, M. G.; Liu, P., Theoretical Study of Methanol Synthesis from Co2 Hydrogenation on Metal-Doped Cu (111) Surfaces. *The Journal of Physical Chemistry C* **2011**, *116*, 248-256.
43. Marcinkowski, M. D.; Murphy, C. J.; Liriano, M. L.; Wasio, N. A.; Lucci, F. R.; Sykes, E. C. H., Microscopic View of the Active Sites for Selective Dehydrogenation of Formic Acid on Cu (111). *Acs Catalysis* **2015**, *5*, 7371-7378.
44. Yoo, J. S.; Abild-Pedersen, F.; Nørskov, J. K.; Studt, F., Theoretical Analysis of Transition-Metal Catalysts for Formic Acid Decomposition. *Acs Catalysis* **2014**, *4*, 1226-1233.
45. Harnos, S.; Onyestyák, G.; Barthos, R.; Štolcová, M.; Kaszonyi, A.; Valyon, J., Novel Cu and Cu 2 in/Aluminosilicate Type Catalysts for the Reduction of Biomass-Derived Volatile Fatty Acids to Alcohols. *Central European Journal of Chemistry* **2012**, *10*, 1954-1962.
46. Onyestyák, G.; Harnos, S.; Badari, C. A.; Drotár, E.; Klébert, S.; Kalló, D., Acetic Acid Hydroconversion over Mono-and Bimetallic Indium Doped Catalysts Supported on Alumina and Silicas of Various Textures. *Open Chemistry* **2015**, *13*, 517-527.
47. Onyestyák, G.; Harnos, S.; Klébert, S.; Štolcová, M.; Kaszonyi, A.; Kalló, D., Selective Reduction of Acetic Acid to Ethanol over Novel Cu2in/Al2o3 Catalyst. *Applied Catalysis A: General* **2013**, *464*, 313-321.

48. Loe, R.; Lavoignat, Y.; Maier, M.; Abdallah, M.; Morgan, T.; Qian, D.; Pace, R.; Santillan-Jimenez, E.; Crocker, M., Continuous Catalytic Deoxygenation of Waste Free Fatty Acid-Based Feeds to Fuel-Like Hydrocarbons over a Supported Ni-Cu Catalyst. *Catalysts* **2019**, *9*, 123.
49. Loe, R.; Santillan-Jimenez, E.; Morgan, T.; Sewell, L.; Ji, Y.; Jones, S.; Isaacs, M. A.; Lee, A. F.; Crocker, M., Effect of Cu and Sn Promotion on the Catalytic Deoxygenation of Model and Algal Lipids to Fuel-Like Hydrocarbons over Supported Ni Catalysts. *Applied Catalysis B: Environmental* **2016**, *191*, 147-156.
50. Santillan-Jimenez, E.; Loe, R.; Garrett, M.; Morgan, T.; Crocker, M., Effect of Cu Promotion on Cracking and Methanation During the Ni-Catalyzed Deoxygenation of Waste Lipids and Hemp Seed Oil to Fuel-Like Hydrocarbons. *Catalysis Today* **2018**, *302*, 261-271.
51. Arend, M.; Nonnen, T.; Hoelderich, W. F.; Fischer, J.; Groos, J., Catalytic Deoxygenation of Oleic Acid in Continuous Gas Flow for the Production of Diesel-Like Hydrocarbons. *Applied Catalysis A: General* **2011**, *399*, 198-204.
52. Blöchl, P. E., Projector Augmented-Wave Method. *Physical review B* **1994**, *50*, 17953.
53. Kresse, G.; Joubert, D., From Ultrasoft Pseudopotentials to the Projector Augmented-Wave Method. *Physical review b* **1999**, *59*, 1758.
54. Kresse, G.; Furthmüller, J., Efficiency of Ab-Initio Total Energy Calculations for Metals and Semiconductors Using a Plane-Wave Basis Set. *Computational materials science* **1996**, *6*, 15-50.
55. Kresse, G.; Furthmüller, J., Efficient Iterative Schemes for Ab Initio Total-Energy Calculations Using a Plane-Wave Basis Set. *Physical review B* **1996**, *54*, 11169.
56. Kresse, G.; Hafner, J., Ab Initio Molecular Dynamics for Liquid Metals. *Physical Review B* **1993**, *47*, 558.
57. Perdew, J. P.; Wang, Y., Accurate and Simple Analytic Representation of the Electron-Gas Correlation Energy. *Physical review B* **1992**, *45*, 13244.
58. Perdew, J. P.; Yue, W., Accurate and Simple Density Functional for the Electronic Exchange Energy: Generalized Gradient Approximation. *Physical review B* **1986**, *33*, 8800.
59. Straumanis, M.; Yu, L., Lattice Parameters, Densities, Expansion Coefficients and Perfection of Structure of Cu and of Cu–in A Phase. *Acta Crystallographica Section A: Crystal Physics, Diffraction, Theoretical and General Crystallography* **1969**, *25*, 676-682.
60. Monkhorst, H. J.; Pack, J. D., Special Points for Brillouin-Zone Integrations. *Physical review B* **1976**, *13*, 5188.
61. Henkelman, G.; Uberuaga, B. P.; Jónsson, H., A Climbing Image Nudged Elastic Band Method for Finding Saddle Points and Minimum Energy Paths. *The Journal of chemical physics* **2000**, *113*, 9901-9904.
62. Henkelman, G.; Jónsson, H., Improved Tangent Estimate in the Nudged Elastic Band Method for Finding Minimum Energy Paths and Saddle Points. *The Journal of chemical physics* **2000**, *113*, 9978-9985.
63. Olsen, R.; Kroes, G.; Henkelman, G.; Arnaldsson, A.; Jónsson, H., Comparison of Methods for Finding Saddle Points without Knowledge of the Final States. *The Journal of chemical physics* **2004**, *121*, 9776-9792.
64. Heyden, A.; Bell, A. T.; Keil, F. J., Efficient Methods for Finding Transition States in Chemical Reactions: Comparison of Improved Dimer Method and Partitioned Rational Function Optimization Method. *The Journal of chemical physics* **2005**, *123*, 224101.
65. Faheem, M.; Suthirakun, S.; Heyden, A., New Implicit Solvation Scheme for Solid Surfaces. *The Journal of Physical Chemistry C* **2012**, *116*, 22458-22462.
66. Klamt, A., Conductor-Like Screening Model for Real Solvents: A New Approach to the Quantitative Calculation of Solvation Phenomena. *The Journal of Physical Chemistry* **1995**, *99*, 2224-2235.
67. Klamt, A.; Jonas, V.; Bürger, T.; Lohrenz, J. C., Refinement and Parametrization of Cosmo-Rs. *The Journal of Physical Chemistry A* **1998**, *102*, 5074-5085.

68. Klamt, A., *Cosmo-Rs: From Quantum Chemistry to Fluid Phase Thermodynamics and Drug Design*; Elsevier, 2005.
69. Zhang, X.; Savara, A.; Getman, R. B., A Method for Obtaining Liquid–Solid Adsorption Rates from Molecular Dynamics Simulations: Applied to Methanol on Pt (111) in H2o. *Journal of Chemical Theory and Computation* **2020**, *16*, 2680-2691.
70. Nitta, T.; Shigetomi, T.; KURO-OKA, M.; Katayama, T., An Adsorption Isotherm of Multi-Site Occupancy Model for Homogeneous Surface. *Journal of chemical engineering of Japan* **1984**, *17*, 39-45.
71. Kozuch, S.; Shaik, S., A Combined Kinetic− Quantum Mechanical Model for Assessment of Catalytic Cycles: Application to Cross-Coupling and Heck Reactions. *Journal of the American Chemical Society* **2006**, *128*, 3355-3365.
72. Kozuch, S.; Shaik, S., Kinetic-Quantum Chemical Model for Catalytic Cycles: The Haber− Bosch Process and the Effect of Reagent Concentration. *The Journal of Physical Chemistry A* **2008**, *112*, 6032-6041.
73. Stegelmann, C.; Andreasen, A.; Campbell, C. T., Degree of Rate Control: How Much the Energies of Intermediates and Transition States Control Rates. *Journal of the American Chemical Society* **2009**, *131*, 8077-8082.
74. Shekhar, M.; Wang, J.; Lee, W.-S.; Williams, W. D.; Kim, S. M.; Stach, E. A.; Miller, J. T.; Delgass, W. N.; Ribeiro, F. H., Size and Support Effects for the Water–Gas Shift Catalysis over Gold Nanoparticles Supported on Model Al2o3 and Tio2. *Journal of the American Chemical Society* **2012**, *134*, 4700-4708.
75. Mudiyanselage, K.; Senanayake, S. D.; Feria, L.; Kundu, S.; Baber, A. E.; Graciani, J.; Vidal, A. B.; Agnoli, S.; Evans, J.; Chang, R., Importance of the Metal–Oxide Interface in Catalysis: In Situ Studies of the Water–Gas Shift Reaction by Ambient-Pressure X-Ray Photoelectron Spectroscopy. *Angewandte Chemie International Edition* **2013**, *52*, 5101-5105.
76. Cui, Y.; Li, Z.; Zhao, Z.; Cybulskis, V. J.; Sabnis, K. D.; Han, C. W.; Ortalan, V.; Schneider, W. F.; Greeley, J.; Delgass, W. N., Participation of Interfacial Hydroxyl Groups in the Water-Gas Shift Reaction over Au/Mgo Catalysts. *Catalysis Science & Technology* **2017**, *7*, 5257-5266.
77. Fu, X.-P.; Guo, L.-W.; Wang, W.-W.; Ma, C.; Jia, C.-J.; Wu, K.; Si, R.; Sun, L.-D.; Yan, C.-H., Direct Identification of Active Surface Species for the Water–Gas Shift Reaction on a Gold–Ceria Catalyst. *Journal of the American Chemical Society* **2019**, *141*, 4613-4623.
78. Hibbitts, D. D.; Loveless, B. T.; Neurock, M.; Iglesia, E., Mechanistic Role of Water on the Rate and Selectivity of Fischer–Tropsch Synthesis on Ruthenium Catalysts. *Angewandte Chemie International Edition* **2013**, *52*, 12273-12278.
79. Gunasooriya, G. K. K.; van Bavel, A. P.; Kuipers, H. P.; Saeys, M., Key Role of Surface Hydroxyl Groups in C–O Activation During Fischer–Tropsch Synthesis. *ACS Catalysis* **2016**, *6*, 3660-3664.
80. De Vrieze, J. E.; Thybaut, J. W.; Saeys, M., Role of Surface Hydroxyl Species in Copper-Catalyzed Hydrogenation of Ketones. *ACS Catalysis* **2018**, *8*, 7539-7548.

Table 1: Vapor phase reaction and activation free energies in eV of all elementary reaction steps in the HDO of propanoic acid over a Cu(111) surface at a temperature of 573 K, a propanoic acid fugacity of 1 bar, and a hydrogen fugacity of 0.1 bar. For corresponding reaction and activation free energies in liquid water and 1,4-dioxane, the correction (based on fluid molecules in the gas phase) is presented, i.e., $\boldsymbol{\Delta G_{solv}^{rxn} = \Delta G_{gas}^{rxn} + \Delta\Delta G_{solv}^{rxn}}$ and $\boldsymbol{\Delta G_{solv}^{\ddagger} = \Delta G_{gas}^{\ddagger} + \Delta\Delta G_{solv}^{\ddagger}}$. The number of * signifies the number of sites a species is adsorbed to.

#	Reaction	Gas		Water		1,4-dioxane	
		ΔG^{rxn}	$\Delta G^{\ddagger}$	$\Delta\Delta G_{solv}^{rxn}$	$\Delta\Delta G_{solv}^{\ddagger}$	$\Delta\Delta G_{solv}^{rxn}$	$\Delta\Delta G_{solv}^{\ddagger}$
0	$CH_3CH_2COOH(g) + * \rightarrow CH_3CH_2COOH*$	0.91	-	0.01	-	-0.02	-
1	$CH_3CH_2COOH* + 3* \rightarrow CH_3CH_2CO*** + OH*$	0.69	1.41	-0.10	-0.22	-0.08	-0.11
2	$CH_3CH_2COOH* + 3* \rightarrow CH_3CHCOOH*** + H*$	0.62	1.08	-0.21	-0.13	-0.12	-0.08
3	$CH_3CH_2CO*** \rightarrow CH_3CH_2* + CO* + *$	0.09	1.04	0.11	0.00	0.08	0.00
4	$CH_3CH_2CO*** + * \rightarrow CH_3CHCO*** + H*$	0.43	1.02	-0.01	-0.04	-0.01	0.00
5	$CH_3CHCOOH*** + * \rightarrow CH_3CHCO*** + OH*$	0.51	0.95	0.10	0.16	0.03	0.07
6	$CH_3CHCOOH*** \rightarrow CH_2CHCOOH* + H* + *$	0.20	0.74	0.23	0.08	0.10	0.06
7	$CH_3CHCOOH*** + * \rightarrow CH_3CCOOH*** + H*$	0.47	1.04	0.08	0.08	0.03	0.03
8	$CH_3CHCO*** \rightarrow CH_3CH** + CO*$	0.14	0.86	0.13	0.03	0.09	0.02
9	$CH_3CHCO*** \rightarrow CH_3CCO** + H*$	0.02	0.74	0.05	0.00	0.03	0.00
10	$CH_3CHCO*** + * \rightarrow CH_2CHCO*** + H*$	0.36	1.12	-0.04	-0.04	-0.05	-0.03
11	$CH_2CHCOOH* + 3* \rightarrow CH_2CHCO*** + OH*$	0.67	1.32	-0.18	-0.16	-0.12	-0.08
12	$CH_2CHCOOH* + 4* \rightarrow CHCHCOOH**** + H*$	0.37	1.10	-0.09	-0.19	-0.07	-0.12
13	$CH_3CCOOH*** \rightarrow CH_3CCO** + OH*$	0.06	0.70	0.07	0.07	0.03	0.06
14	$CH_3CCO** \rightarrow CH_3C* + CO*$	0.25	1.05	0.06	-0.05	0.05	-0.03
15	$CH_2CHCO*** \rightarrow CH_2CH* + CO* + *$	-0.19	0.76	0.11	-0.01	0.08	0.00
16	$CH_2CHCO*** + 2* \rightarrow CHCHCO**** + H*$	0.27	0.99	-0.01	-0.06	0.01	-0.02
17	$CHCHCOOH**** + * \rightarrow CHCHCO**** + OH*$	0.56	1.28	-0.10	-0.07	-0.04	0.02
18	$CHCHCO**** \rightarrow CHCH*** + CO*$	-0.49	0.68	0.09	-0.03	0.05	-0.05
19	$CHCH*** + H* \rightarrow CH_2CH* + 3*$	0.04	0.79	0.03	0.08	0.02	0.07
20	$CH_2CH* + H* \rightarrow CH_2CH_2* + *$	-0.56	1.02	-0.01	-0.01	0.01	0.00
21	$CH_2C* + H* \rightarrow CH_2CH* + *$	-0.18	0.61	-0.03	-0.08	-0.03	-0.06
22	$CH_3C* + * \rightarrow CH_2C* + H*$	0.09	1.02	-0.02	-0.12	-0.02	-0.09
23	$CH_2CH* + H* \rightarrow CH_3CH**$	-0.03	0.73	0.07	-0.04	0.07	-0.01
24	$CH_3C* + H* \rightarrow CH_3CH**$	-0.12	0.53	0.02	0.02	0.02	0.02

25	$CH_3CH^{**} + H^* \rightarrow CH_3CH_2^* + 2^*$	-0.49	0.49	-0.01	-0.05	0.00	-0.04
26	$CH_3CH_2^* + H^* \rightarrow CH_3CH_3^* + *$	-0.96	0.45	0.01	-0.02	0.01	-0.01
27	$CH_3CH_2^* + * \rightarrow CH_2CH_2^* + H^*$	-0.04	0.56	-0.07	-0.09	-0.05	-0.07
28	$CH_3CH_2COOH^* + 2^* \rightarrow CH_3CH_2COO^{**} + H^*$	-0.40	0.39	-0.08	-0.09	-0.04	-0.04
29	$CH_3CH_2COO^{**} \rightarrow CH_3CH_2^* + CO_2^*$	1.03	1.97	0.19	-0.09	0.13	-0.03
30	$CH_3CH_2COO^{**} + 2^* \rightarrow CH_3CHCOO^{***} + H^*$	1.16	1.92	-0.17	-0.27	-0.08	-0.10
31	$CH_3CHCOOH^{***} + * \rightarrow CH_3CHCOO^{***} + H^*$	0.15	0.89	-0.04	-0.04	0.00	0.01
32	$CH_3CHCOOH^{***} + * \rightarrow CH_3CH^{**} + COOH^{**}$	1.22	1.68	0.09	0.04	0.06	0.01
33	$CH_3CHCOO^{***} \rightarrow CH_3CH^{**} + CO_2^*$	0.36	1.06	0.36	0.11	0.21	0.05
34	$CH_3CHCOO^{***} + * \rightarrow CH_3CCOO^{***} + H^*$	0.80	1.51	-0.12	0.01	-0.04	0.02
35	$CH_3CCOOH^{***} + * \rightarrow CH_3CCOO^{***} + H^*$	0.48	1.49	-0.24	-0.41	-0.07	-0.14
36	$CH_3CCOOH^{***} \rightarrow CH_3C^* + COOH^{**}$	0.88	1.56	-0.01	-0.06	0.01	-0.02
37	$CH_2CHCOOH^* + 2^* \rightarrow CH_2CH^* + COOH^{**}$	1.05	1.71	-0.20	-0.26	-0.11	-0.13
38	$CH_3CCOO^{***} \rightarrow CH_3C^* + CO_2^* + ^*$	-0.32	0.66	0.46	0.11	0.24	0.03
39	$COOH^{**} \rightarrow CO_2^* + H^*$	-0.72	0.89	0.23	-0.04	0.15	0.00
40	$COOH^{**} \rightarrow CO^* + OH^*$	-0.57	0.20	0.13	0.07	0.07	0.04
41	$H_2O^* + * \rightarrow OH^* + H^*$	0.01	1.00	0.05	0.08	-0.01	0.03
42	$CH_3CH_3 + * \rightarrow CH_3CH_3^*$	1.08	-	0.06	-	0.05	-
43	$CH_2CH_2 + * \rightarrow CH_2CH_2^*$	0.85	-	0.01	-	0.01	-
44	$H_2O + * \rightarrow H_2O^*$	0.94	-	-0.11	-	-0.07	-
45	$CO_2 + * \rightarrow CO_2^*$	0.60	-	0.06	-	0.04	-
46	$CHCH + 3^* \rightarrow CHCH^{***}$	-0.49	-	0.03	-	0.02	-
47	$CO + * \rightarrow CO^*$	0.60	-	-0.01	-	0.00	-
48	$H_2^* + * \rightarrow H^* + H^*$	-0.20	0.56	-0.07	-0.05	-0.08	-0.06
49	$CH_3CH_2COOH^* + H^* \rightarrow CH_3CH_2COHOH^{**}$	1.45	1.29	-0.06	-0.18	0.01	-0.14
50	$CH_3CH_2COOH^* + H^* \rightarrow CH_3CH_2CHOHO^*$	0.44	1.02	-0.03	-0.09	0.02	-0.02
51	$CH_3CH_2CO^{***} + H^* \rightarrow CH_3CH_2CHO^* + 3^*$	-0.15	0.49	0.08	0.05	0.04	0.02
52	$CH_3CH_2COO^{**} + H^* \rightarrow CH_3CH_2CHOO^{***}$	1.03	1.48	0.07	-0.02	0.07	0.01
53	$CH_3CHCOOH^{***} + H^* \rightarrow CH_3CHCOHOH^* + 3^*$	0.46	0.69	0.09	0.09	0.06	0.08
54	$CH_3CH_2COHOH^{**} \rightarrow CH_3CH_2COH^* + OH^*$	-0.18	0.13	0.03	0.05	-0.04	0.00
55	$CH_3CH_2COHOH^{**} + H^* \rightarrow CH_3CH_2CHOHOH^* + 2^*$	-0.98	-0.03	0.06	0.08	0.01	0.01
56	$CH_3CH_2CHOHO^* + * \rightarrow CH_3CH_2CHO^* + OH^*$	0.10	0.47	0.00	-0.06	-0.05	-0.07

57	$CH_3CH_2CHO^* + H^* \rightarrow CH_3CH_2CH_2O^* + *$	-0.36	0.49	0.05	-0.06	0.04	-0.02
58	$CH_3CH_2CHO^* + H^* \rightarrow CH_3CH_2CHOH^{**}$	0.60	0.92	0.00	-0.02	0.02	-0.03
59	$CH_3CH_2CHOO^{***} + H^* \rightarrow CH_3CH_2CHOHO^* + 3^*$	-0.19	0.83	-0.02	-0.08	-0.01	-0.03
60	$CH_3CHCOHOH^* + 3^* \rightarrow CH_3CHCOH^{***} + OH^*$	0.32	1.91	-0.08	-0.12	-0.12	-0.10
61	$CH_3CHCO^{***} + H^* \rightarrow CH_3CHCHO^{***} + *$	-0.48	0.44	-0.01	-0.01	0.00	-0.01
62	$CH_3CHCO^{***} + H^* \rightarrow CH_3CHCOH^{***} + *$	0.27	0.83	-0.08	0.08	-0.09	0.06
63	$CH_3CH_2COH^* + H^* \rightarrow CH_3CH_2CHOH^{**}$	-0.14	0.66	0.01	-0.15	0.02	-0.14
64	$CH_3CH_2CHOHOH^* + 2^* \rightarrow CH_3CH_2CHOH^{**} + OH^*$	0.67	1.64	-0.01	-0.01	-0.04	-0.04
65	$CH3CHCOH^{***} + H^* \rightarrow CH3CH2COH^* + 3^*$	-0.12	0.73	0.17	0.13	0.14	0.11
66	$CH3CH2CH2O^* + H^* \rightarrow CH3CH2CH2OH^* + *$	0.08	0.99	-0.03	0.05	-0.01	0.04
67	$CH_3CH_2CHOH^{**} + H^* \rightarrow CH_3CH_2CH_2OH^* + 2^*$	-0.88	0.37	0.02	-0.11	0.01	-0.05
68	$CH_3CHCHO^{***} + H^* \rightarrow CH_3CH_2CHO^* + 3^*$	-0.10	0.57	0.10	0.12	0.05	0.09
69	$CH_3CH_2CO^{***} + H^* \rightarrow CH_3CH_2COH^* + 3^*$	0.59	0.84	0.08	0.07	0.05	0.05
70	$CH_3CH_2CH_2O^* + CH_3CH_2CO^{***} \rightarrow CH_3CH_2COOCH_2CH_2CH_3^* + 3^*$	-0.62	0.70	0.00	0.01	0.04	0.04
71	$CH_3CHCOHOH^* + H^* \rightarrow CH_3CH_2COHOH^{**}$	0.37	0.45	0.06	-0.01	0.06	0.00
72	$CH_3CHCOHOH^* + H^* + * \rightarrow CH_3CHCHOHOH^{***}$	0.40	0.98	-0.05	0.02	-0.04	0.02
73	$CH_3CHCHOHOH^{***} + H^* \rightarrow CH_3CH_2CHOHOH^* + 3^*$	-1.01	0.52	0.17	0.01	0.12	0.01
74	$CH_3CHCOH^{***} + H^* \rightarrow CH_3CHCHOH^* + 3^*$	-0.58	0.61	0.15	0.04	0.13	0.03
75	$CH_3CHCHO^{***} + H^* \rightarrow CH_3CHCHOH^* + 3^*$	0.17	0.78	0.07	0.02	0.04	0.04
76	$CH_3CHCHO^{***} + H^* \rightarrow CH_3CHCH_2O^{***} + *$	0.62	0.94	0.14	0.03	0.10	0.03
77	$CH_3CHCH_2O^{***} + H^* \rightarrow CH_3CH_2CH_2O^* + 3^*$	-1.08	0.39	0.01	0.01	-0.01	0.01
78	$CH_3CHCH_2O^{***} + H^* \rightarrow CH_3CHCH_2OH^{**} + 2^*$	-0.08	0.87	-0.10	-0.19	-0.08	-0.09
79	$CH_3CHCHOH^* + H^* \rightarrow CH_3CH_2CHOH^{**}$	0.32	0.71	0.04	0.01	0.03	0.00
80	$CH_3CHCHOH^* + H^* \rightarrow CH_3CHCH_2OH^{**}$	0.37	0.90	-0.03	0.05	-0.03	0.04
81	$CH_3CHCH_2OH^{**} + H^* \rightarrow CH_3CH_2CH_2OH^* + 2^*$	-0.92	0.57	0.09	-0.05	0.06	-0.03
82	$CH_3CH_2CHOHO^* + H^* \rightarrow CH_3CH_2CHOHOH^* + *$	0.03	0.89	0.02	-0.02	0.01	0.00

83	$CH_3CH_2CO^{***} + CH_3CH_2^* \rightarrow CH_3CH_2COCH_2CH_3^* + 3^*$	-1.12	0.77	0.01	-0.07	-0.02	-0.05
84	$CH_3CHCHOHOH^{***} \rightarrow CH_3CHCHOH^* + OH^* + *$	-0.67	0.71	0.12	-0.06	0.06	-0.09
85	$CH_3CH_2CH_2OH + * \rightarrow CH_3CH_2CH_2OH^*$	0.82	-	0.01	-	-0.01	-
86	$CH_3CH_2CHO + * \rightarrow CH_3CH_2CHO^*$	0.92	-	0.02	-	-0.01	-
87	$CH_3CH_2COOCH_2CH_2CH_3 + * \rightarrow CH_3CH_2COOCH_2CH_2CH_3^*$	0.87	-	0.00	-	0.03	-
88	$CH_3CH_2COCH_2CH_3 + * \rightarrow CH_3CH_2COCH_2CH_3^*$	0.88	-	0.03	-	0.00	-
89	$H_2 + * \rightarrow H_2^*$	0.78	-	0.04	-	0.04	-
90	$C_4H_8O_2 + * \rightarrow C_4H_8O_2^*$	0.48	-	-0.04	-	-0.02	-

Table 2. Solvent effect on the stability of various adsorbed species in the HDO of PAc to ethane and ethylene over a Cu(111) catalyst surface model at a reaction temperature of 573 K. $\Delta\Delta G_{solv}$ indicates the difference in the adsorption free energy of the corresponding intermediate in the presence and the absence of the solvent. Asterisk (*) represents a surface adsorption site and multiple asterisks are indicative of the number of occupied active sites.

Adsorbed species	**$\Delta\Delta G_{solv}$ (eV)**	
	Water	**1,4-Dioxane**
CH_2C*	0.09	0.07
CH_2CH*	0.04	0.02
CH_2CH_2*	0.01	0.01
CH_2CHCO***	-0.07	-0.05
$CH_2CHCOOH$*	0.06	0.00
CH_3C*	0.09	0.07
CH_3CCO**	0.02	0.02
CH_3CCOO***	-0.32	-0.13
CH_3CCOOH***	-0.09	-0.07
CH_3CH**	0.09	0.07
CH_3CH_2*	0.07	0.05
$CH_3CH_2CH_2O$*	0.05	0.02
$CH_3CH_2CH_2OH$*	0.01	-0.01
CH_3CH_2CHO*	0.02	-0.01
CH_3CH_2CHOH**	0.01	0.00
CH_3CH_2CHOHO*	-0.03	-0.02
$CH_3CH_2CHOHOH$*	-0.02	-0.03
CH_3CH_2CHOO***	0.00	0.01
CH_3CH_2CO***	-0.05	-0.03
$CH_3CH_2COCH_2CH_3$*	0.03	0.00
CH_3CH_2COH*	0.01	0.00
CH_3CH_2COHOH**	-0.07	-0.03
CH_3CH_2COO**	-0.06	-0.05
$CH_3CH_2COOCH_2CH_2CH_3$*	0.00	0.03
CH_3CH_2COOH*	0.01	-0.02
CH_3CH_3*	0.06	0.05
CH_3CHCH_2O***	0.06	0.04
CH_3CHCH_2OH**	-0.06	-0.05
CH_3CHCHO***	-0.07	-0.04
$CH_3CHCHOH$*	-0.02	-0.01
$CH_3CHCHOHOH$***	-0.18	-0.13
CH_3CHCO***	-0.05	-0.02

CH_3CHCOH***	-0.15	-0.12
$CH_3CHCOHOH$*	-0.12	-0.07
CH_3CHCOO***	-0.21	-0.11
$CH_3CHCOOH$***	-0.19	-0.12
CHCH***	0.03	0.02
CHCHCO****	-0.07	-0.03
CHCHCOOH****	-0.02	-0.06
CO*	-0.01	0.00
CO_2*	0.06	0.04
COOH**	-0.19	-0.13
H*	-0.02	-0.02
H_2*	0.04	0.04
H_2O*	-0.11	-0.07
$C_4H_8O_2$*	-0.04	-0.02
OH*	-0.05	-0.07

Table 3: TOFs (s^{-1}) and the number of surface species per surface metal atom ($\boldsymbol{\theta}$) of the most abundant surface intermediates in the vapor phase, liquid water, and 1,4-dioxane over a Cu(111) surface at a propanoic acid fugacity of 1 bar, and a H_2 fugacity of 0.1 bar at temperatures of 473 K and 573 K. The number of * signifies the number of sites a species is adsorbed to. Free surface coverage denoted by $\boldsymbol{\theta}$*.

Phase	T (K)	TOF (s^{-1})	$\boldsymbol{\theta}$*	$\boldsymbol{\theta_{CH_3CH_2COO}}$**
Gas	473	6.7×10^{-9}	0.75	0.12
	573	8.1×10^{-6}	0.94	0.03
Water	473	3.6×10^{-8}	0.51	0.24
	573	9.0×10^{-5}	0.84	0.08
1,4-dioxane	473	1.6×10^{-8}	0.58	0.21
	573	3.2×10^{-5}	0.87	0.07

Table 4: Product selectivity under gas and liquid phase conditions at a temperature of 573 K, a propanoic acid fugacity of 1 bar and a hydrogen fugacity of 0.1 bar over a Cu(111) surface. For simulations in liquid water and 1,4-dioxane results are shown for the default and ±10% increased/decreased Cu cavity radius.

	Gas	Water			1,4-dioxane		
		default	-10%	+10%	default	-10%	+10%
DCN	0.16	0.03	0.02	0.04	0.11	0.08	0.11
DCX	0.79	0.94	0.95	0.94	0.85	0.89	0.86
CH_3CH_2CHO	0.05	0.02	0.03	0.02	0.03	0.03	0.03

Table 5: Degree of rate control for various steps over a Cu(111) surfaces under gas and liquid phase reactions conditions at a temperature of 573 K, a propanoic acid fugacity of 1 bar and a hydrogen fugacity of 0.1 bar. In addition to liquid phase simulation results obtained with default Cu cavity radius, results with ±10% increased/reduced Cu cavity radius are also presented.

	Gas	**Water**			**1,4-dioxane**		
		default	**-10%**	**+10%**	**default**	**-10%**	**+10%**
Step 2	0.06	-	-	-	0.02	0.01	0.01
Step 5	0.14	0.02	0.01	0.02	0.09	0.06	0.09
Step 29	0.24	0.32	0.39	0.34	0.26	0.24	0.26
Step 30	0.16	0.02	-	0.01	0.09	0.09	0.07
Step 31	0.10	-	-	-	0.02	0.01	0.01
Step 33	0.26	0.60	0.56	0.60	0.46	0.46	0.50

Table 6: Degree of thermodynamic rate control for $CH_3CH_2COO^{**}$ over a Cu(111) surfaces under gas and liquid phase conditions at a temperature of 573 K, a propanoic acid fugacity of 1 bar and a hydrogen fugacity of 0.1 bar. In addition to liquid phase simulation results obtained with default Cu cavity radius, results with ±10% increased/reduced Cu cavity radius are also presented.

	Gas	**Water**			**1,4-dioxane**		
		default	**-10%**	**+10%**	**default**	**-10%**	**+10%**
$CH_3CH_2COO^{**}$	-0.19	-0.38	-0.47	-0.29	-0.35	-0.28	-0.30

Table 7: Degree of selectivity control (Xsc) for reaction steps that impact the DCN, DCX, and propionaldehyde (denoted as CHO) production pathways in the vapor phase at a temperature of 573 K, a propanoic acid partial pressure of 1 bar and a hydrogen partial pressure of 0.1 bar over a Cu(111) surface.

Elementary reactions		Xsc		
		DCN	**DCX**	**CHO**
2	$CH_3CH_2COOH^* + 3^* \rightarrow CH_3CHCOOH^{***} + H^*$	0.07	-0.02	0.03
5	$CH_3CHCOOH^{***} + ^* \rightarrow CH_3CHCO^{***} + OH^*$	0.61	-0.16	0.49
7	$CH_3CHCOOH^{***} + ^* \rightarrow CH_3CCOOH^{***} + H^*$	0.13	-0.03	0.02
	DCN:			
8	$CH_3CHCO^{***} \rightarrow CH_3CH^{**} + CO^*$	0.03	0.00	-0.08
9	$CH_3CHCO^{***} \rightarrow CH_3CCO^{**} + H^*$	0.09	0.00	-0.26
14	$CH_3CCO^{**} \rightarrow CH_3C^* + CO^*$	0.08	0.00	-0.22
	DCX:			
29	$CH_3CH_2COO^{**} \rightarrow CH_3CH_2^* + CO_2^*$	-0.24	0.06	-0.24
30	$CH_3CH_2COO^{**} + 2^* \rightarrow CH_3CHCOO^{***} + H^*$	-0.13	0.04	-0.14
31	$CH_3CHCOOH^{***} + ^* \rightarrow CH_3CHCOO^{***} + H^*$	-0.16	0.04	-0.14
33	$CH_3CHCOO^{***} \rightarrow CH_3CH^{**} + CO_2^*$	-0.30	0.08	-0.29
	CH_3CH_2CHO:			
1	$CH_3CH_2COOH^* + 3^* \rightarrow CH_3CH_2CO^{***} + OH^*$	0.00	0.00	0.08
4	$CH_3CH_2CO^{***} + ^* \rightarrow CH_3CHCO^{***} + H^*$	-0.02	0.00	0.05
50	$CH_3CH_2COOH^* + H^* \rightarrow CH_3CH_2CHOHO^*$	-0.01	-0.01	0.17
56	$CH_3CH_2CHOHO^* + ^* \rightarrow CH_3CH_2CHO^* + OH^*$	0.00	0.00	0.02
61	$CH_3CHCO^{***} + H^* \rightarrow CH_3CHCHO^{***} + ^*$	-0.09	0.00	0.27
68	$CH_3CHCHO^{***} + H^* \rightarrow CH_3CH_2CHO^* + 3^*$	-0.08	0.00	0.24

Table 8: Degree of selectivity control (Xsc) for reaction steps that impact the DCN, DCX, and propionaldehyde (denoted as CHO) production pathways in liquid 1,4-dioxane at a temperature of 573 K, a propanoic fugacity of 1 bar and a hydrogen fugacity of 0.1 bar over a Cu(111) surface.

Elementary reactions		Xsc		
		DCN	**DCX**	**CHO**
2	$CH_3CH_2COOH^* + 3^* \rightarrow CH_3CHCOOH^{***} + H^*$	0.04	-0.01	0.01
5	$CH_3CHCOOH^{***} + ^* \rightarrow CH_3CHCO^{***} + OH^*$	0.58	-0.09	0.33
7	$CH_3CHCOOH^{***} + ^* \rightarrow CH_3CCOOH^{***} + H^*$	0.23	-0.03	0.03
	DCN:			
8	$CH_3CHCO^{***} \rightarrow CH_3CH^{**} + CO^*$	0.01	0.00	-0.05
9	$CH_3CHCO^{***} \rightarrow CH_3CCO^{**} + H^*$	0.05	0.00	-0.17
14	$CH_3CCO^{**} \rightarrow CH_3C^* + CO^*$	0.06	0.00	-0.21
	DCX:			
29	$CH_3CH_2COO^{**} \rightarrow CH_3CH_2^* + CO_2^*$	-0.26	0.04	-0.26
30	$CH_3CH_2COO^{**} + 2^* \rightarrow CH_3CHCOO^{***} + H^*$	-0.07	0.01	-0.08
31	$CH_3CHCOOH^{***} + ^* \rightarrow CH_3CHCOO^{***} + H^*$	-0.05	0.01	-0.04
33	$CH_3CHCOO^{***} \rightarrow CH_3CH^{**} + CO_2^*$	-0.50	0.08	-0.48
	CH_3CH_2CHO:			
1	$CH_3CH_2COOH^* + 3^* \rightarrow CH_3CH_2CO^{***} + OH^*$	-0.01	-0.01	0.30
4	$CH_3CH_2CO^{***} + ^* \rightarrow CH_3CHCO^{***} + H^*$	-0.02	0.00	0.07
50	$CH_3CH_2COOH^* + H^* \rightarrow CH_3CH_2CHOHO^*$	-0.01	-0.01	0.18
51	$CH_3CH_2CO^{***} + H^* \rightarrow CH_3CH_2CHO^* + 3^*$	0.00	0.00	0.02
56	$CH_3CH_2CHOHO^* + ^* \rightarrow CH_3CH_2CHO^* + OH^*$	0.00	0.00	0.01
61	$CH_3CHCO^{***} + H^* \rightarrow CH_3CHCHO^{***} + ^*$	-0.02	0.00	0.06
68	$CH_3CHCHO^{***} + H^* \rightarrow CH_3CH_2CHO^* + 3^*$	-0.08	0.00	0.28

Table 9: Degree of selectivity control (Xsc) for reaction steps that impact the DCN, DCX, and propionaldehyde (denoted as CHO) production pathways in liquid water at a temperature of 573 K, a propanoic acid fugacity of 1 bar and a hydrogen fugacity of 0.1 bar over a Cu(111) surface.

Elementary reactions		Xsc		
		DCN	DCX	CHO
	DCN:			
2	$CH_3CH_2COOH^* + 3^* \rightarrow CH_3CHCOOH^{***} + H^*$	0.01	0.00	0.00
3	$CH_3CH_2CO^{***} \rightarrow CH_3CH_2^* + CO^* + *$	0.02	0.00	-0.02
4	$CH_3CH_2CO^{***} + * \rightarrow CH_3CHCO^{***} + H^*$	0.01	0.00	-0.01
5	$CH_3CHCOOH^{***} + * \rightarrow CH_3CHCO^{***} + OH^*$	0.46	-0.02	0.08
7	$CH_3CHCOOH^{***} + * \rightarrow CH_3CCOOH^{***} + H^*$	0.37	-0.01	0.02
8	$CH_3CHCO^{***} \rightarrow CH_3CH^{**} + CO^*$	0.01	0.00	-0.01
9	$CH_3CHCO^{***} \rightarrow CH_3CCO^{**} + H^*$	0.03	0.00	-0.04
14	$CH_3CCO^{**} \rightarrow CH_3C^* + CO^*$	0.05	0.00	-0.07
	DCX:			
29	$CH_3CH_2COO^{**} \rightarrow CH_3CH_2^* + CO_2^*$	-0.32	0.02	-0.32
30	$CH_3CH_2COO^{**} + 2^* \rightarrow CH_3CHCOO^{***} + H^*$	0.00	0.00	-0.01
33	$CH_3CHCOO^{***} \rightarrow CH_3CH^{**} + CO_2^*$	-0.62	0.04	-0.60
	CH_3CH_2CHO:			
1	$CH_3CH_2COOH^* + 3^* \rightarrow CH_3CH_2CO^{***} + OH^*$	0.04	-0.02	0.63
50	$CH_3CH_2COOH^* + H^* \rightarrow CH_3CH_2CHOHO^*$	0.00	0.00	0.18
51	$CH_3CH_2CO^{***} + H^* \rightarrow CH_3CH_2CHO^* + 3^*$	-0.05	0.00	0.08
56	$CH_3CH_2CHOHO^* + * \rightarrow CH_3CH_2CHO^* + OH^*$	0.00	0.00	0.02
61	$CH_3CHCO^{***} + H^* \rightarrow CH_3CHCHO^{***} + *$	-0.01	0.00	0.01
68	$CH_3CHCHO^{***} + H^* \rightarrow CH_3CH_2CHO^* + 3^*$	-0.05	0.00	0.07

Table 10: Degree of selectivity control (Xsc) for CH_3CH_2COO** that impacts the DCN, DCX and propionaldehyde production pathways in various reaction environments at a temperature of 573 K, a propanoic acid fugacity of 1 bar and a hydrogen fugacity of 0.1 bar over a Cu(111) surface. In addition to liquid phase simulation results obtained with default Cu cavity radius, results with ±10% increased/reduced Cu cavity radius are also presented.

CH_3CH_2COO**		**Gas**	**Water**			**1,4-dioxane**		
			default	**-10%**	**+10%**	**default**	**-10%**	**+10%**
Xsc	**DCN**	-0.03	-0.16	-0.20	-0.12	-0.10	-0.08	-0.08
	DCX	0.01	0.01	0.01	0.01	0.02	0.01	0.02
	CH_3CH_2CHO	-0.07	-0.15	-0.20	-0.12	-0.15	-0.14	-0.14

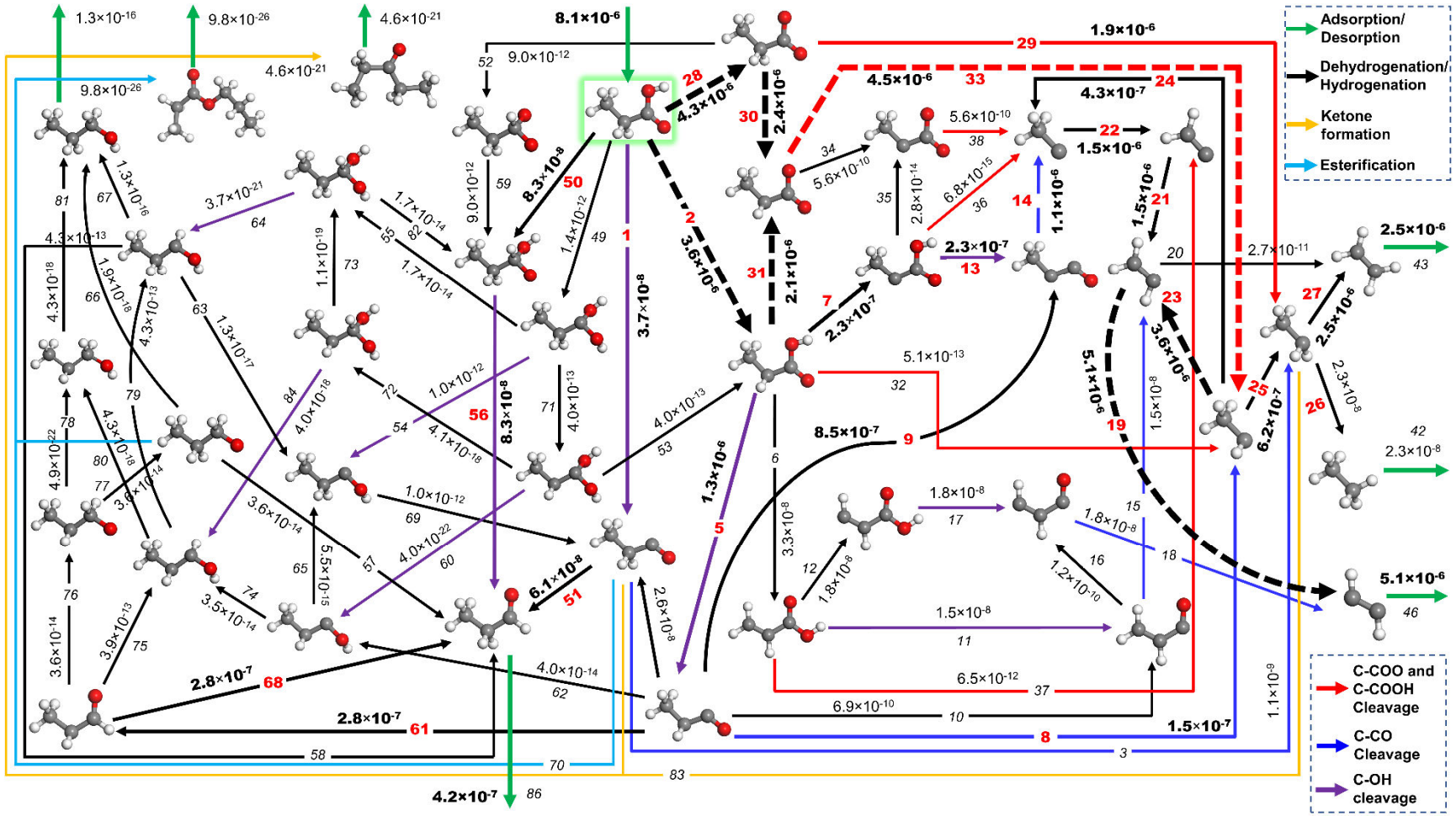

Figure 1: Reaction network with turnover frequencies (TOFs (s^{-1})) of various elementary steps in vapor phase at a temperature of 573 K, a propanoic acid gas phase partial pressure of 1 bar, and a hydrogen partial pressure of 0.1 bar. Color codes are shown in the insets. For convenience, the dominant pathway shown by bold, dashed arrows.

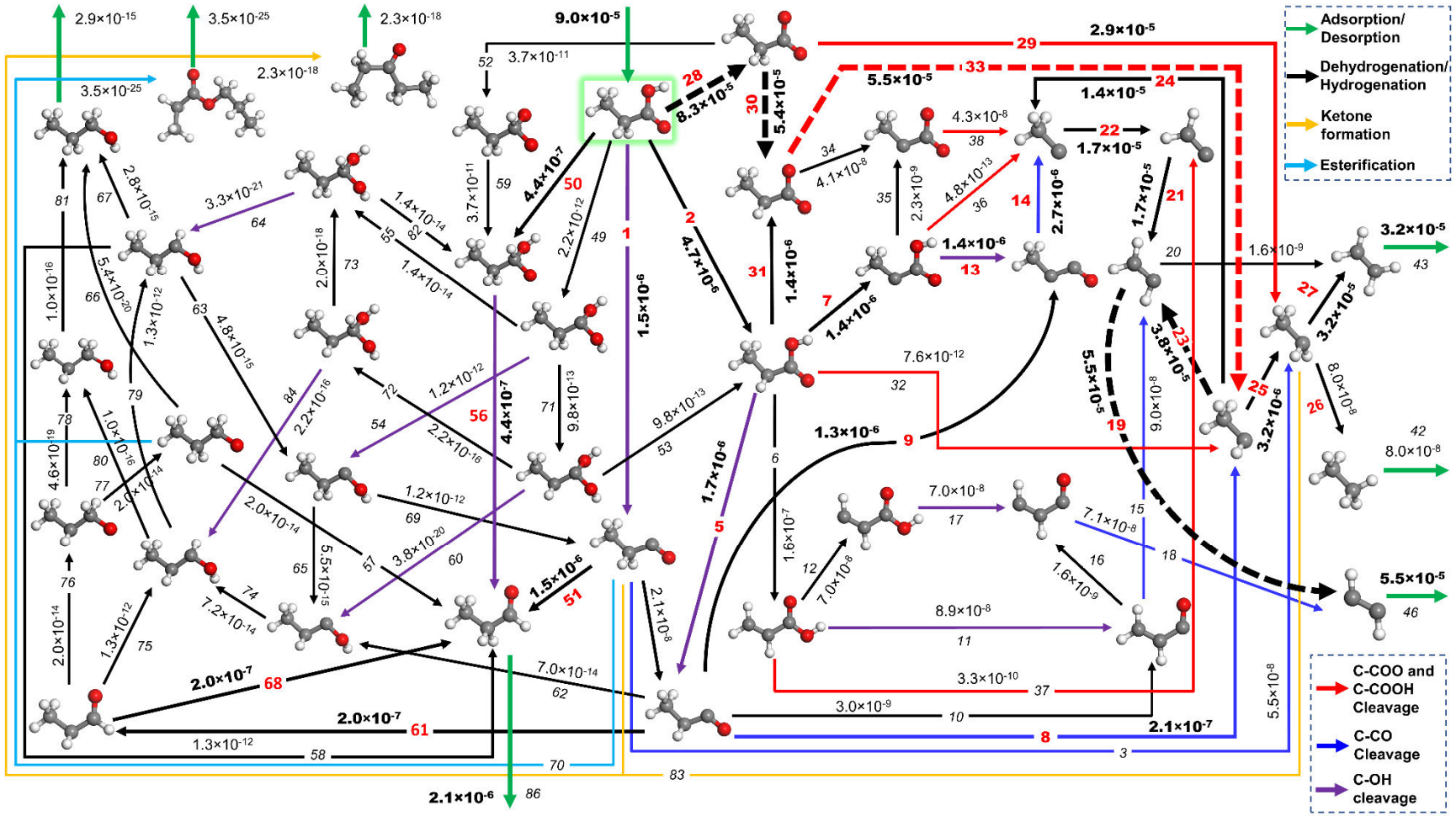

Figure 2: Reaction network with turnover frequencies (TOFs (s^{-1})) of various elementary steps in liquid water at a temperature of 573 K, a propanoic acid fugacity of 1 bar, and a hydrogen fugacity of 0.1 bar. Color codes are shown in the insets. For convenience, the dominant pathway shown by bold, dashed arrows.

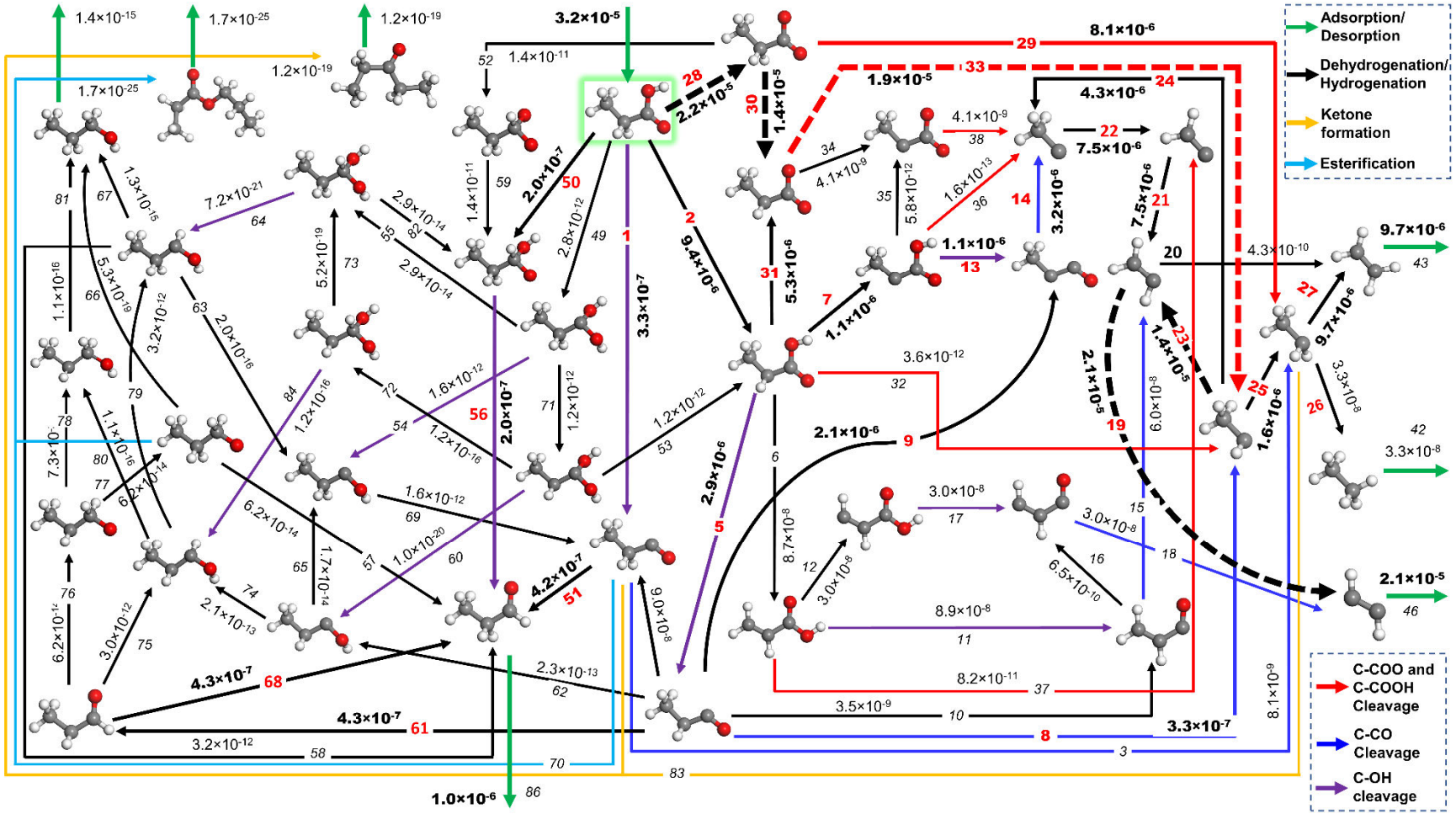

Figure 3: Reaction network with turnover frequencies (TOFs (s^{-1})) of various elementary steps in liquid 1,4-dioxane at a temperature of 573 K, a propanoic acid fugacity of 1 bar, and a hydrogen fugacity of 0.1 bar. Color codes are shown in the insets. For convenience, the dominant pathway shown by bold, dashed arrows.

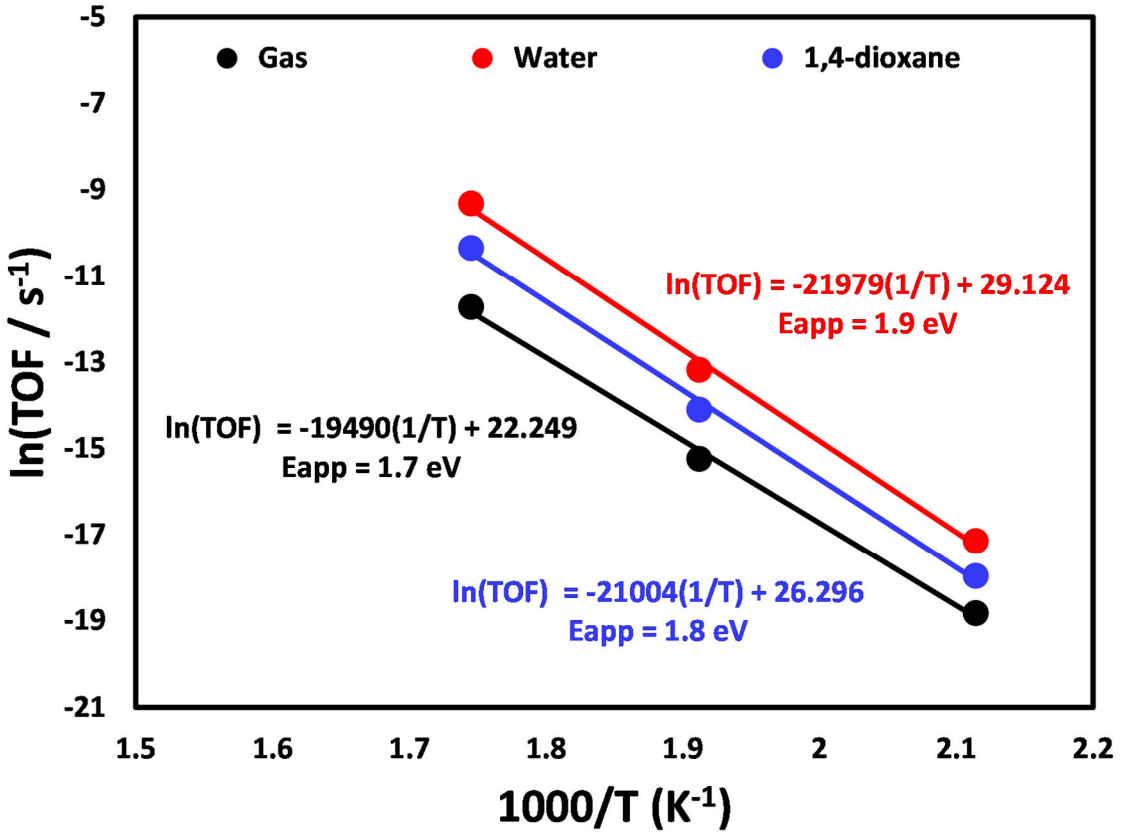

Figure 4: Arrhenius plot for the HDO of propanoic acid in various reaction environments in the temperature range of 473-573 K at a propanoic acid fugacity of 1 bar and a hydrogen fugacity of 0.1 bar over a Cu(111) surface.

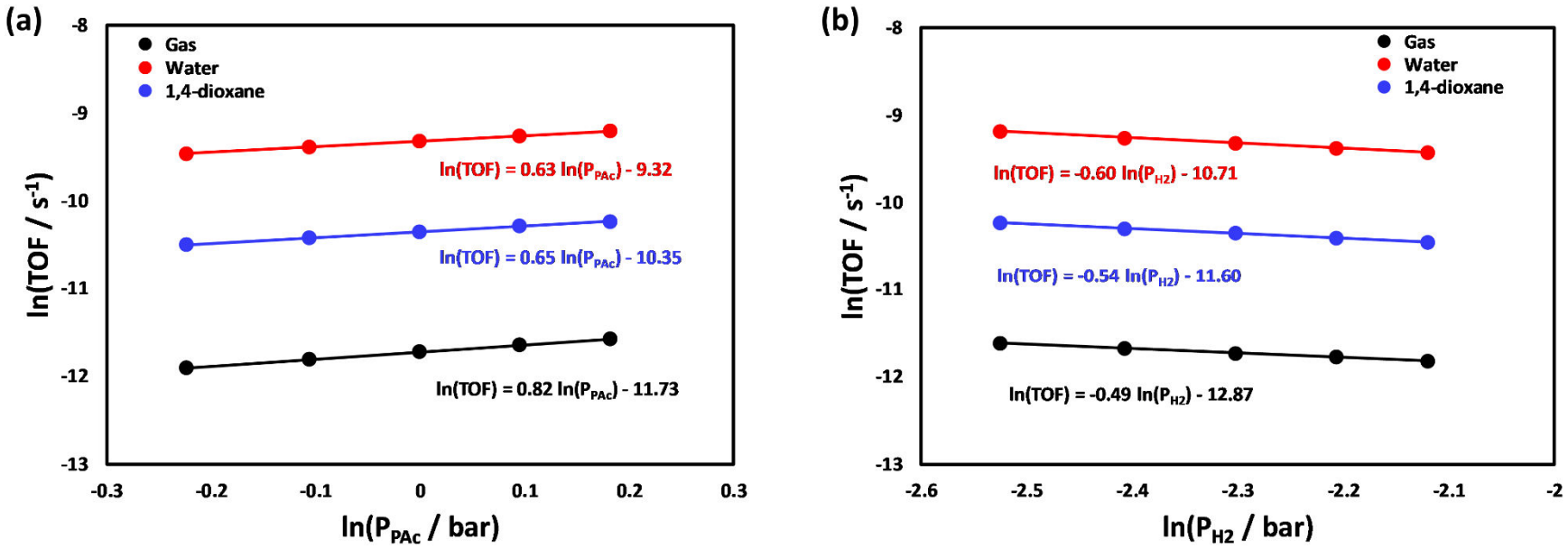

Figure 5: Reaction orders (slope of the corresponding graph lines) in various reaction environments of (a) propanoic acid and (b) H_2 at a temperature of 573 K, a propanoic acid fugacity of 1 bar, and a hydrogen fugacity of 0.1 bar over a Cu(111) surface.

TOC Graphic: